

# Design and Operation of FACT – The First G-APD Cherenkov Telescope

---

H. Anderhub<sup>a</sup>, M. Backes<sup>b</sup>, A. Biland<sup>a</sup>, V. Boccone<sup>c</sup>, I. Braun<sup>a</sup>, T. Bretz<sup>a,d\*</sup>, J. Buß<sup>b</sup>,  
F. Cadoux<sup>c</sup>, V. Commichau<sup>a</sup>, L. Djambazov<sup>a</sup>, D. Dorner<sup>e,c</sup>, S. Einecke<sup>b</sup>,  
D. Eisenacher<sup>e</sup>, A. Gendotti<sup>a</sup>, O. Grimm<sup>a</sup>, H. von Gunten<sup>a</sup>, C. Haller<sup>a</sup>, D. Hildebrand<sup>a</sup>,  
U. Horisberger<sup>a</sup>, B. Huber<sup>a1</sup>, K.-S. Kim<sup>a2</sup>, M. L. Knoetig<sup>a</sup>, J.-H. Köhne<sup>b</sup>,  
T. Krähenbühl<sup>a</sup>, B. Krumm<sup>b</sup>, M. Lee<sup>a2</sup>, E. Lorenz<sup>a3</sup>, W. Luster<sup>a</sup>, E. Lyard<sup>c</sup>,  
K. Mannheim<sup>e</sup>, M. Meharga<sup>c</sup>, K. Meier<sup>e</sup>, T. Montaruli<sup>c</sup>, D. Neise<sup>b</sup>, F. Nessi-Tedaldi<sup>a</sup>,  
A.-K. Overkemping<sup>b</sup>, A. Paravac<sup>e</sup>, F. Pauss<sup>a</sup>, D. Renker<sup>a4</sup>, W. Rhode<sup>b</sup>, M. Ribordy<sup>d</sup>,  
U. Röser<sup>a</sup>, J.-P. Stucki<sup>a</sup>, J. Schneider<sup>a</sup>, T. Steinbring<sup>e</sup>, F. Temme<sup>b</sup>, J. Thaele<sup>b</sup>,  
S. Tobler<sup>a</sup>, G. Viertel<sup>a</sup>, P. Vogler<sup>a</sup>, R. Walter<sup>c</sup>, K. Warda<sup>b</sup>, Q. Weitzel<sup>a\*</sup>, M. Zänglein<sup>e</sup>

<sup>a</sup>ETH Zurich, Switzerland – Institute for Particle Physics, Schafmattstr. 20, 8093 Zurich

<sup>b</sup>Technische Universität Dortmund, Germany

Experimental Physics 5, Otto-Hahn-Str. 4, 44221 Dortmund

<sup>c</sup>University of Geneva, Switzerland

ISDC Data Center for Astrophysics, Chemin d'Ecogia 16, 1290 Versoix

Département de Physique Nucléaire et Corpusculaire, Quai Ernest-Ansermet 24, 1211 Geneva

<sup>d</sup>EPF Lausanne, Switzerland – Laboratory for High Energy Physics, 1015 Lausanne

<sup>e</sup>Universität Würzburg, Germany

Institute for Theoretical Physics and Astrophysics, Emil-Fischer-Str. 31, 97074 Würzburg,

<sup>1</sup>Also at: University of Zurich, Physik-Institut, 8057 Zurich, Switzerland

<sup>2</sup>Also at: Kyungpook National University, Center for High Energy Physics, 702-701 Daegu, Korea

<sup>3</sup>Also at: Max-Planck-Institut für Physik, 80805 Munich, Germany

<sup>4</sup>Also at: Technische Universität München, 85748 Garching, Germany

**ABSTRACT:** The First G-APD Cherenkov Telescope (FACT) is designed to detect cosmic gamma-rays with energies from several hundred GeV up to about 10 TeV using the Imaging Atmospheric Cherenkov Technique. In contrast to former or existing telescopes, the camera of the FACT telescope is comprised of solid-state Geiger-mode Avalanche Photodiodes (G-APD) instead of photo-multiplier tubes for photo detection. It is the first full-scale device of its kind employing this new technology. The telescope is operated at the Observatorio del Roque de los Muchachos (La Palma, Canary Islands, Spain) since fall 2011. This paper describes in detail the design, construction and operation of the system, including hardware and software aspects. Technical experiences gained after one year of operation are discussed and conclusions with regard to future projects are drawn.

**KEYWORDS:** Gamma astronomy; Cherenkov detectors; Geiger-mode avalanche photo diode.

---

\*Corresponding authors: thomas.bretz@phys.ethz.ch, qweitzel@phys.ethz.ch

---

## Contents

|  |           |
|--|-----------|
| <b>1. Introduction</b>                             | <b>3</b>  |
| <b>2. System Overview</b>                          | <b>4</b>  |
| <b>3. Telescope</b>                                | <b>6</b>  |
| 3.1 Mount and Drive                                | 6         |
| 3.2 Pointing Calibration                           | 6         |
| 3.3 Reflector                                      | 7         |
| 3.3.1 Re-workings and Spectral Reflectivities      | 7         |
| 3.3.2 Focal Lengths and Point Spread Functions     | 8         |
| 3.3.3 Alignment                                    | 9         |
| 3.4 Light-pulser                                   | 10        |
| <b>4. Camera</b>                                   | <b>11</b> |
| 4.1 Mechanical Layout                              | 11        |
| 4.2 Sensor Compartment                             | 12        |
| 4.3 Readout and Trigger Electronics                | 16        |
| 4.3.1 Preamplifier and Trigger Signal Conditioning | 16        |
| 4.3.2 Trigger Unit                                 | 17        |
| 4.3.3 Trigger Master Board                         | 18        |
| 4.3.4 Digitization                                 | 19        |
| 4.4 Power, Cooling and Auxiliary Systems           | 20        |
| 4.4.1 Power Conversion and Distribution            | 20        |
| 4.4.2 Bias Voltage Supply                          | 21        |
| 4.4.3 Interlock System, Remote Control and Heaters | 22        |
| 4.4.4 Cooling System                               | 23        |
| 4.4.5 Slow Control Board                           | 24        |
| 4.4.6 Shutter                                      | 24        |
| <b>5. Online Software and Data Storage</b>         | <b>25</b> |
| 5.1 Overview                                       | 25        |
| 5.2 Sub-components                                 | 25        |
| 5.2.1 System Configuration                         | 25        |
| 5.2.2 Inter-communication                          | 25        |
| 5.2.3 Data Storage                                 | 26        |
| 5.2.4 Dimctrl                                      | 27        |
| 5.2.5 Graphical User Interface                     | 27        |
| 5.2.6 Smartfact                                    | 28        |
| 5.2.7 Automation/Scheduling                        | 28        |
| 5.2.8 Electronic Logbook                           | 29        |

|  |           |
|--|-----------|
| 5.2.9 Individual Programs                                    | 29        |
| 5.2.10 Feedback  | 29        |
| 5.2.11 Ratecontrol   | 30        |
| 5.3 Data Acquisition   | 30        |
| 5.4 Data Taking Procedure                                    | 31        |
| 5.5 Data Center  | 32        |
| <b>6. Conclusions</b>  | <b>33</b> |
| 6.1 Problems during Construction, Final Tests, and Operation | 33        |
| 6.2 Achievements   | 34        |
| 6.3 Possible Future Improvements and Outlook                 | 35        |

---

## 1. Introduction

For more than two decades, Imaging Atmospheric Cherenkov Telescopes (IACT) have been very successful in observing cosmic gamma-ray sources at very high energies (VHE, about 50 GeV to 100 TeV) [1]. More than 100 sources have been detected, including galactic, as well as extragalactic, objects like Supernova Remnants or Active Galactic Nuclei (AGN). The observed gamma-ray flux is energy and source dependent and can be highly variable. Combining the datasets with observations at other wavelengths (e.g. radio or X-ray data) allows to study cosmic particle acceleration and radiation emission mechanisms. To detect variability on long time scales and understand the flaring behavior of AGN, continuous monitoring for several months or years is necessary. This can be achieved by robust and small telescopes [2], complementary to the large-scale arrays serving many tasks.

Cosmic-ray induced particle cascades generate Cherenkov light in the atmosphere [3] with a broad spectrum peaking between 300 nm and 350 nm. These light flashes have a typical photon density at ground of a few up to several hundred photons per square-meter on nano-second time scales. If recorded with an imaging device, the image topology allows to reconstruct energy and direction of the primary particle and to determine its type [4]. The latter allows the suppression of the strong hadron induced background exceeding the rate of gamma induced air-showers typically by  $10^4$  to  $10^5$ .

In order to achieve the goal of long-term monitoring as good as possible, operation during moonlit nights is mandatory. While for dark nights the intensity of the diffuse night-sky background is of the order of  $10 \text{ MHz/cm}^2$  [5, 6], for moonlit nights it can be three or four orders of magnitude higher.

The Cherenkov light is collected by means of a large reflector with an area of several to a few hundred square meters, focusing it onto a fast and sensitive camera. To keep the costs and the point-spread function low, reflectors are segmented. Due to the small opening angle of Cherenkov light, the reflector has to be oriented towards the shower origin. This can be achieved, for example, by an alt-azimuth mount able to track any position on the sky.

Up to now, all cameras of IACTs have been built with photomultiplier tubes (PMT), but during the last years novel solid-state photosensors have been developed [7]. Primarily, Geiger-mode Avalanche Photodiodes (G-APD, notation used in this paper for entire sensor subdivided in cells) have the potential to replace PMTs in gamma-ray astronomy. They offer a high gain ( $10^5$  to  $10^6$ ) and can be operated under much brighter light conditions allowing observations during moon time. Their single photon counting capability is a powerful tool for the signal calibration, and their compactness and their low operational voltage ( $< 100 \text{ V}$ ) simplify the camera design. The photon detection efficiency (PDE) of commercially available G-APDs is already at the level of the best PMTs, and is still improved by the manufacturers.

In order to demonstrate the advantages of novel light sensors for VHE gamma-ray astronomy, the First G-APD Cherenkov Telescope (FACT) has been developed featuring a complete camera based on G-APDs. After successful tests with a small (36 pixels) prototype module in summer and fall 2009 [8] and a re-design, the full-size camera (1440 pixels) has been constructed. In fall 2011 the device has been shipped to La Palma (Canary Islands, Spain), and installed on an existing telescope mount at the Observatorio del Roque de los Muchachos (ORM, 2200 m a.s.l.). In October



**Figure 1.** Photograph of the FACT telescope at the Observatorio del Roque de los Muchachos on La Palma (Canary Islands, Spain). At the top right the camera is visible (white cylinder), including the cables for power and communication connected at its back. The cables are fixed along the telescope masts and, together with the cables for the drive system, guided through a cable duct to the counting house (the container at the left). In the middle of the reflector where one mirror is missing, the light pulser and the video-camera are installed. The cooling unit is inside the metal box placed on the telescope platform.

2011, few hours after installation, first air-shower images have been recorded. The system has been running almost every night since then and several source observations have already been conducted for its commissioning.

## 2. System Overview

The FACT experiment consists of several sub-systems serving different purposes during operation. In this section an overview of the setup is given with links to detailed descriptions following in the next sections. All hardware components are either located on the telescope mount or in a counting room a few meters away. Figure 1 shows a photograph of the telescope. In figure 2 a schematic diagram of the system is presented. The installations at the ORM are located on the site of the Major Atmospheric Gamma-ray Imaging Cherenkov Telescopes (MAGIC, [9]), from which power

is provided. The Davies-Cotton reflector and the camera are installed on a movable mount. A fast light pulser for calibration purposes is situated in the mirror dish (see section 3). A video-camera, installed next to the light pulser, allows to take pictures of the telescope-camera to check the environment conditions and to calibrate the pointing using the reflection of bright stars (c.f. section 3.2).

The camera has a total field-of-view of  $4.5^\circ$  and is comprised of 1440 individual pixels equipped with a G-APD and a light concentrator each (see section 4). All channels are read out individually. The required electronics for analog processing, digitization, and triggering is integrated into the camera body. Trigger signals, as well as a precise clock signal, are distributed from the trigger master board to 40 digitizer boards (see section 4.3). The environmental conditions inside the camera, such as temperature and humidity, and all supplied voltages and drawn currents from the internal power-supplies are monitored by a slow control board. Communication and data readout is based on standard Ethernet connections. Waste heat, dissipated by the electronics and internal power supplies, is conducted through a water-circulation system (see section 4.4). Its pump is placed on the telescope platform to limit the length of the connecting tubes. The operation voltage of the photo sensors, the so-called bias voltage, is supplied to groups of four and five sensors and provided by a dedicated power supply located in the counting room. During data taking this voltage can be regularly adjusted in order to keep the gain of the sensors stable (see section 4.4). The counting room also hosts the power supplies for the camera and the drive motors, as well as the control system of the latter. An interlock system ensures that the camera is only powered when the cooling unit is operating. In order to allow remote operations, both the power unit of the camera and the interlock system can be accessed via Ethernet. Several computers are employed for data ac-

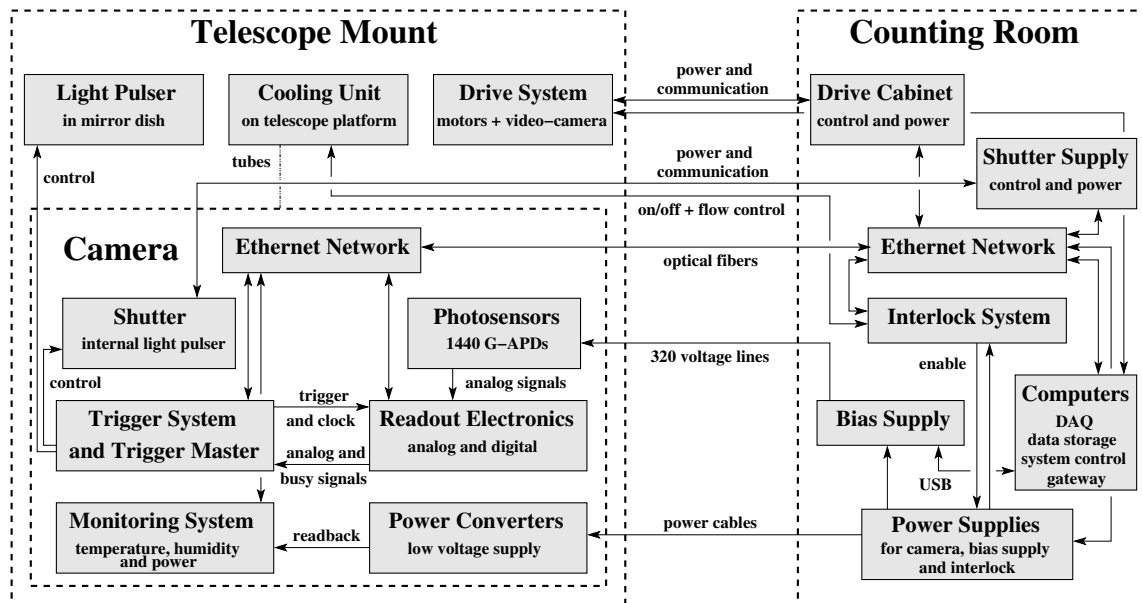


**Figure 2.** Schematic overview of the different sub-systems (gray boxes) constituting the FACT telescope. The arrows indicate electrical connections for power, signal transfer or communication. All components are located either in the counting room (right) or on the telescope mount (left). Hardware belonging to the camera is represented as a subgroup of the telescope mount.



quisition, temporary data storage and system control via online software programs (see section 5). A graphical user interface is provided for the telescope operator. Each day the raw data from the last night is automatically transferred from the telescope site to a data center in mainland Europe, where it is processed and prepared for the offline analysis. In order to obtain preliminary results quickly, an automated analysis is running on the on-site computers.

### **3. Telescope**

#### **3.1 Mount and Drive**

As a mount, the former HEGRA CT3 telescope, c.f. [10, 11], is used. The alt-azimuth mount is made of a massive steel structure driven by the originally installed industrial worm gears (ZAE-Antriebssysteme GmbH & Co KG,  $i=46$ ). All other components were upgraded to a drive system similar to the one in use for both MAGIC telescopes [12]. Due to the more than ten times lower telescope weight (compared to MAGIC), and thus reduced requirements on the motor power, 1 kW motors (Bosch, MSK 070-D-0300) with a maximum torque of 8 Nm are employed. Their power is transmitted by planetary gears (Wittenstein alpha, LP-120-M02-30-111,  $i=30$ ) to the worm gears connected on both axes. Planetary gears and worm gears are connected by a transmission shaft with a bevel gear allowing movements in case of failure with a standard curtain crank. As motor controllers, Bosch IndraDrive HCS 02 are used. They are controlled from a Programmable Logic Controller (PLC, Bosch SPS L 40) via Profibus connection. High-level commands are transmitted via Ethernet from a standard PC. The position control loop is closed by shaft-encoders, one on each axis (Heidenhain ROQ 425 EnDat 01). The PLC program and the PC program are almost identical to the MAGIC version. The main differences are due to different interlock systems. A simple joystick, connected via cable to the PLC, is available to move the telescope without PC. All components are watertight and classified as IP 67 (housing) or IP 64 (shafts). An additional splash water protection is installed.

#### **3.2 Pointing Calibration**

To correct for the imprecision of a real telescope mount, a pointing calibration is performed. The resulting pointing model allows to convert calculated source positions to real command values. For its determination, the telescope is pointed to a sequence of many bright stars, and the position of each reflected image on the camera surface is evaluated w.r.t. their nominal position in the camera center. To determine the camera center, eight Light Emitting Diodes (LED) are mounted in a circle around the camera center at the camera edge. Covering the sky homogeneously with such calibration measurements the pointing correction can be parametrized depending on the nominal pointing position. Once a pointing model has been computed and applied, the calibration measurements can also be used to evaluate the current pointing quality (the residuals).

Before the start of operation, a first pointing model has been determined. Measurements after almost one year of operation have shown that the pointing accuracy during tracking has only marginally degraded and is still better than 30 arcsec.

### 3.3 Reflector

The existing reflector has the sphere-like shape of a so-called Davies-Cotton mirror arrangement [13] in which individual mirrors are placed at their focal distance to the focal point and oriented towards a point at twice the focal length. This combines the advantages of the correct focal distance with an ideal alignment, and is cheaper than a single-reflector design. The former glass mirrors have been exchanged with the mirrors originally built for an upgrade of HEGRA CT 1. The new mirrors are entirely made out of aluminum, with a honeycomb inlay between the front and the back plates. They are of hexagonal shape, covering an area of  $0.317 \text{ m}^2$  each. Being comprised of 30 of such mirrors, the total reflective surface of the telescope amounts to  $9.51 \text{ m}^2$  (about 10% more than for HEGRA CT 3).

#### 3.3.1 Re-workings and Spectral Reflectivities

The more than twelve year old mirrors were re-machined using diamond-milling by the company LT Ultra Precision Technology GmbH. Subsequently, they were coated with  $\text{SiO}_2$  at the Fraunhofer Institute for Manufacturing Technology and Applied Materials Research. Within a methane atmosphere of a few mbar, silicon was deposited to the mirrors with a sputtering technique and afterwards oxidized. Thus,  $\text{SiO}_2$  was built up with some admixture of carbon from the dissociation of methane. The coating thickness has a major influence on the spectral reflectivity by thin layer interference and should be less than 120 nm, taking the spectral shape of the Cherenkov radiation into account. The specular reflectivity of all mirrors was measured to be constant within 4% over the surface of every single mirror. The coating of the mirrors was conducted in two batches affecting the coating thickness and thus the spectral reflectivity. The different charges form two classes of mean reflectivity as depicted in figure 3.

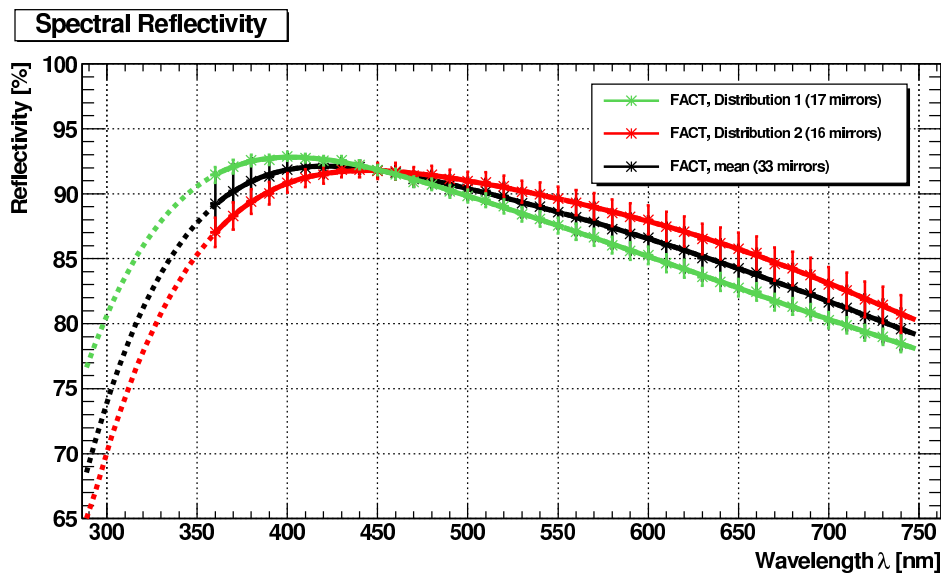


**Figure 3.** Spectral reflectivity for all 33 measured mirrors. The two distributions (green, red) originate from batches which were coated independently. The black curve is the average of all mirrors. Error bars represent the measured spread. The interpolation (solid) and extrapolation (dotted) was done by fitting a 6th order polynomial.



In order to determine the coating thickness, the reflectivity of a single mirror has been re-measured with a PerkinElmer LAMBDA 650 UV/Vis Spectrophotometer, which offers a wider wavelength range of 190 nm – 900 nm compared to 360 nm – 740 nm of the former measurements. The wavelength accuracy is  $\pm 0.15$  nm. The measurements have been conducted in steps of 1 nm between 200 nm and 800 nm. These results and the average of the corresponding batch measured previously are shown in figure 4. Clearly an inter-instrument offset can be seen, probably due to slightly different integration angles for the specular reflections. In order to cross-check the shape of the extension of the batch mirror measurements to lower wavelengths (green dashed line, used for simulations) a scaling factor of 1.0375 has been applied to the PerkinElmer measurement.

The interference minimum measured occurred at 272 nm. Assuming an incidence angle of  $30^\circ$ , the refractive index of  $\text{SiO}_2$  at 272 nm wavelength is reported as 1.589 for crystalline silica and 1.50 for fused silica [14]. Hence, the coating thickness  $d$  is estimated as 90.2 nm and 96.4 nm.

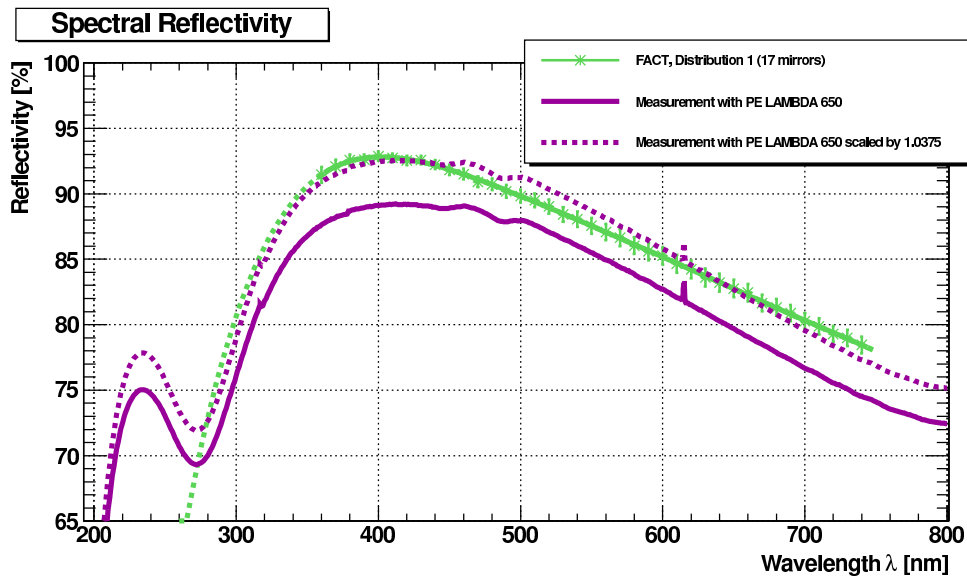


**Figure 4.** Spectral reflectivity for the first batch of mirrors (green) compared to the measurement of a single mirror using a different setup (down to 200 nm, solid purple). An instrumental offset between both measurements is visible, well described by applying a scale factor (dashed purple).

### 3.3.2 Focal Lengths and Point Spread Functions

After the milling process some tension might persist inside the aluminum plate and cause distortions to the spherical symmetry of the mirror resulting in two different focal lengths for two orthogonal directions. In order to measure the distance and size of the spot with the smallest distortion, a test setup was built. As a point source, a red LED was placed behind a 1 mm pinhole at twice the expected focal distance. Pictures of the image were taken from the front side of a backside illuminated screen at several distances with a commercial Sony  $\alpha 550$  camera with an image resolution of  $4,592 \times 3,056$  pixels and equipped with a SIGMA MAKRO 105 mm F2.8 EX DG objective lens.

For each background subtracted and noise suppressed image, the smallest ellipse containing 95% of the light is fitted. Plotting the area of the ellipse versus distance allows to find the point

of the smallest distortion. In this way, the ideal distance of the mirror to the focal plane, called focal length in the following, and the size of the spot containing 95% of the reflected light, in the following called point-spread function (PSF) is defined.

Figure 5 (right) shows the resulting distribution of focal lengths depicting a very small spread of 9 mm ( $< 2\%$ ) around the average focal length of 4.889 m. Figure 5 (left) shows the distribution of the measured point-spread functions. The mean of the distribution of spot sizes measured at  $2F$  is  $(15.95 \pm 6.73) \text{ mm}^2$ . The spot size at their focal distance is four times smaller. That means that nearly all of the mirror facets focus 95% of the reflected light in an area well below one quarter of the size of one pixel ( $19.54 \text{ mm}^2$ ).

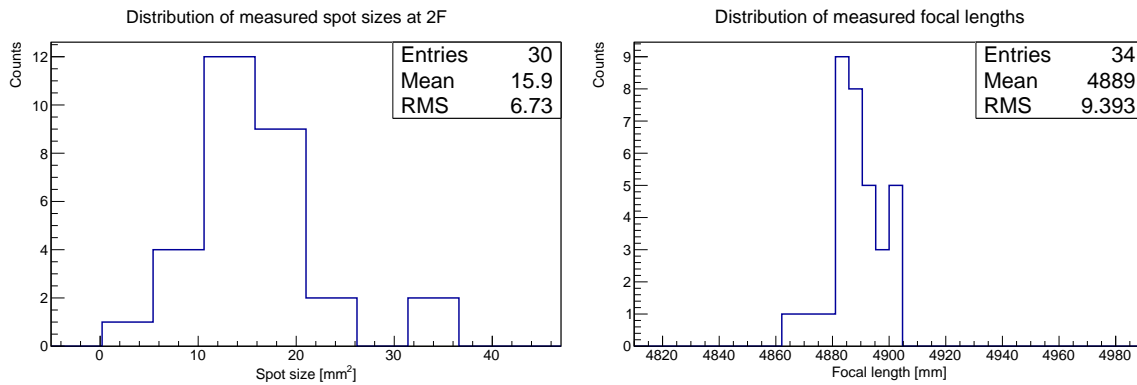


**Figure 5.** Left: Distribution of the area in square-millimeter of an ellipse containing 95% of the light at  $2F$  for the 30 mirror facets. The corresponding value at their measured focal length is thus four times smaller. The focal length was determined as the point at which the area gets minimal. Right: Corresponding distribution of the focal length (for 30+4 facets).

### 3.3.3 Alignment

In order to be able to align all mirrors individually, each mirror is equipped with a tripod which allows to alter the  $z$ -position at three points. For the on-site alignment of the mirrors, an equipment has been set up at a distance of twice the desired focal length along the optical axis of the telescope, when the camera was not yet mounted. To define the optical axis, a laser was shot from the center of the reflector through the center of the camera mounting ring. The alignment device consisted of a laser and a screen, both installed at the same distance to the optical axis. A universal joint allowed to orient the device towards each individual mirror. For a better sensitivity the screen was monitored with a CCD camera also displaying a cross hair for better alignment. With this method a typical alignment error of the center of the light distribution of  $\pm 1.5 \text{ mm}$  on the focal plane was achieved. Admittedly, the point-spread function is currently compiled from two mirror batches about 4.5 mm apart on the focal plane. These two batches correspond to the upper and lower half of the mirrors and result from the bending of the camera holding structure which was used to determine the optical axis while the reflector was turned upside-down for an easier access to the upper half of the mirrors. A new device allowing alignment also with the camera mounted is under construction.

### 3.4 Light-pulser

For test and calibration purposes the telescope uses two light-pulser systems. In this section the so-called external light-pulser is described, situated in the center of the mirror dish. A second system, the internal light-pulser, is installed on the inside of the camera shutter (see section 4.1). Both light pulsers are operated with similar electronics.

The external light-pulser features a total of 18 Light Emitting Diodes (LED) from Avago Technologies, type HLMP-CB-1A-XY, with a dominant wavelength of 470 nm, i.e. blue light, and a viewing angle of  $15^\circ$  defined as the full width half maximum of their radiation pattern. Both, the electronics as well as the LEDs are mounted in a commercial aluminum die-cast case. In figure 6 a front view (left) and an inside view (right) are presented. The external light-pulser is controlled by the trigger master board inside the camera (see section 4.3) via four Low Voltage Differential Signaling lines (LVDS). Standard RJ-45 Ethernet cables are used to transmit the LVDS signals. During standard data taking, only the two central LEDs visible in figure 6 (left) are used.

The light-pulser electronics features a feedback circuit in order to stabilize the light yield of the LEDs over the maximum temperature range expected at the ORM ( $-10^\circ\text{C}$  up to  $+40^\circ\text{C}$ , approximately). For this purpose, an additional LED is mounted inside the case coupled to a silicon pin-photodiode (Hamamatsu S 5821). Depending on the output of the photodiode, the current supply of all (18+1) LEDs is regulated. The amplitude set point is generated by the trigger master board as a pulse-duty factor signal and transmitted via one of the LVDS lines. An additional on-board signal generator allows to operate the light pulser without the trigger master board for debugging purposes.

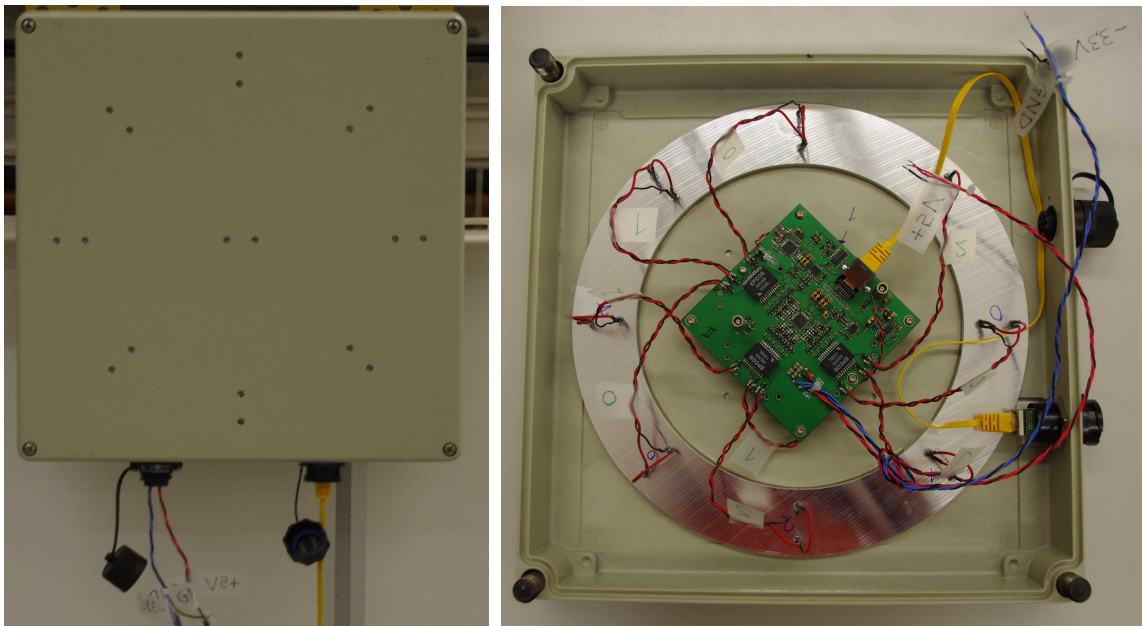


**Figure 6.** Photographs of the external light pulser. Left: Front view showing the geometrical configuration of the LEDs during a test installation in the laboratory; at the bottom also the connectors for power and control can be seen. Right: The electronics board inside the box supplying and stabilizing the LEDs.

## 4. Camera

### 4.1 Mechanical Layout

The camera has a diameter of 53 cm and a length of 81 cm. It consists of two mechanically separated compartments, one for the photo sensors and one for the readout electronics (see figure 7). The sensor compartment has a plexiglass protection window and light concentrators on the entrance side, with the G-APDs being glued onto the backside of the concentrators (for details, see section 4.2). To avoid power dissipation from the electronics to the sensor compartment, an insulation is installed. This baffle plate is made of 23 mm Styrofoam (CORAPAN<sup>®</sup> AL 85), laminated on both sides by 1 mm aluminum and equipped with cable connector boards. The sensor compartment has its own water-tight cover (2 mm-thick aluminum cylinder, not shown in figure 7) and can be detached from the rest of the camera.

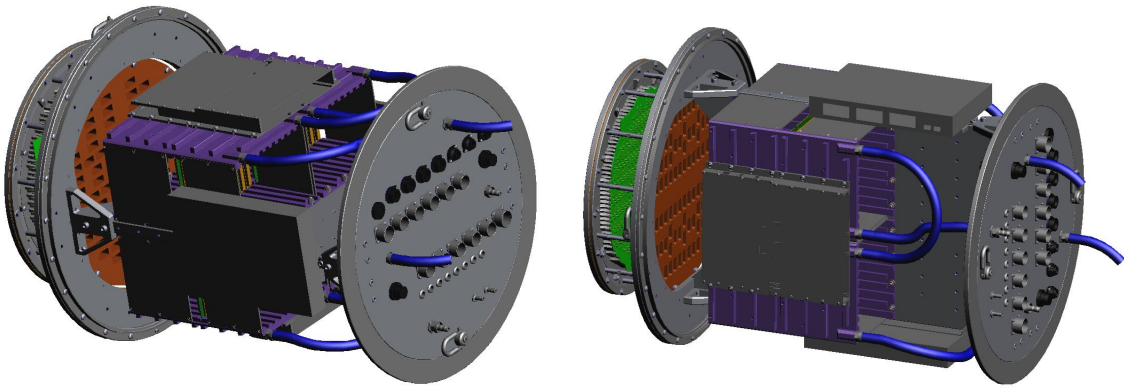


**Figure 7.** CAD drawing of the camera mechanics without cover and shutter. Left/Right: Cooling plate in horizontal/vertical position. The sensor compartment can be seen to the left of the large electronics compartment in the middle, and the backplane to the right. In blue the tubes for the cooling system are indicated.

Most of the electronics boards are arranged in four water-cooled crates with  $2 \times 10$  slots each. These crates constitute the biggest fraction of the electronics compartment which is subdivided in two parts by a 24 mm aluminum plate. This plate serves as mechanical holding structure as well as heat sink (see also section 4.4.4). On both sides of the camera, an Ethernet switch is installed. In the back part of the camera, the internal power supplies, two on each side, are installed. Four more electronics boards with individual aluminum covers are mounted on top of the crates. All aluminum pieces of the camera are alodined to protect them against corrosion and to keep their thermal and electrical conductivity. Figure 8 (left) shows the camera during the construction phase with the cooling plate in horizontal position. For stability reasons, the camera is mounted such that for the parked telescope the cooling plate is oriented in vertical position (see figure 8, right). Similar to the sensor compartment, also the electronics compartment has a 2 mm-thick cylindrical cover imposed, varnished with white baking paint. All connectors for power and communication are located on the backside of the camera. Dust and water tightness according to IP 67 are ensured by using o-ring sealings and dedicated cable feedthroughs and connectors. A Gore-Tex<sup>®</sup> valve is employed for pressure compensation.



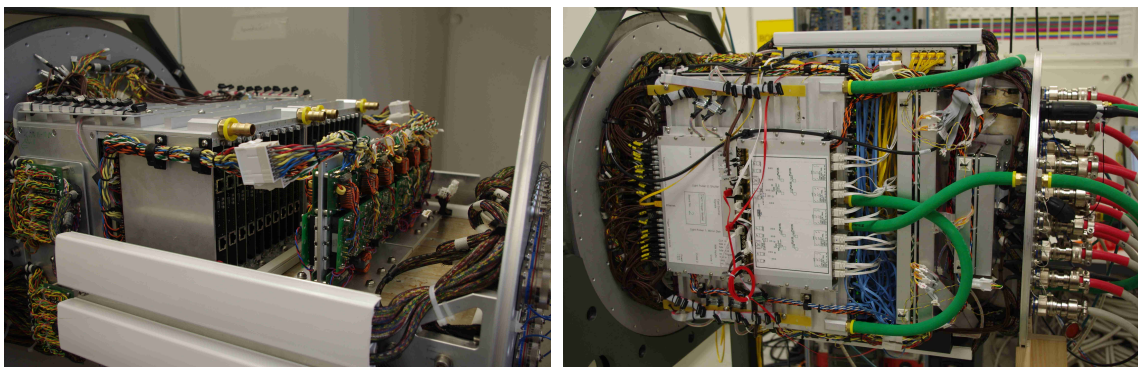


**Figure 8.** Photographs taken during the construction of the camera. Left: Two crates mounted on the (horizontal) cooling plate with plugged-in electronics boards and power supplies (without cover). Right: Fully equipped and cabled electronics compartment (vertical mounting) including cooling tubes; on the top one of the network switches is visible, in the foreground the cover boxes of the trigger master board and one of the fast signal distribution boards; the cables attached from outside to the backplane of the camera can be seen on the right.

In front of the sensor compartment there is a shutter which can be opened and closed remotely (not visible in figure 7 or 8, see section 4.4.6). It consists of two halves, both equipped with D-shaped PMMA (Polymethyl Methacrylate, plexiglass) sheets on their inner side. A total of eight LED pairs is glued onto the edges of each sheet. This is the so-called internal light-pulsar. In contrast to the external one (c.f. section 3.4), the corresponding electronics board is placed inside the camera. The PMMA sheets are sandblasted on the side facing the camera such that the light of the LEDs is scattered onto the pixels. This system can be used for test measurements during daytime when the shutter is closed.

Including the shutter and the internal light pulsar, the camera has a total weight of 152 kg.

## 4.2 Sensor Compartment

A total of 1595 G-APDs (Hamamatsu MPPC S10362-33-50C [15]) were purchased for the project (not only for the camera, but also for test setups). The sensors have an active area of  $3\text{ mm} \times 3\text{ mm}$  evenly subdivided into 3600 cells. The active area is enclosed by a ceramic packaging and protected by a thin (typically 0.3 mm) epoxy-resin layer with a refractive index between 1.49 and 1.54. With the resin, the sensitivity for incoming photons has a lower cut-off around 320 nm, matching approximately the cut-off introduced also by the light concentrators (see figure 9). The dark count rate per sensor is of the order of a few MHz at room temperature, thus below the NSB rate even during darkest nights (c.f. section 1). The G-APDs are operated at a gain of  $7.5 \cdot 10^5$ , with a peak PDE of  $\sim 33\%$  between 450 nm and 500 nm and a crosstalk probability of  $\sim 13\%$ . The latter is defined as the probability that a primary avalanche will trigger a second or more cells (see e.g. [16]). Provided that an incoming photon is detected by the sensor, and assuming that there is no crosstalk or saturation, one avalanche is equivalent to a single photon signal (photon equivalent, p.e.).

To get a homogeneous response over the camera, the G-APDs were sorted according to their nominal operation voltage. Those requiring a very low or very high voltage were not used. After

this selection step, 1535 sensors remained with a voltage range from 70.64 V to 71.63 V (for an operation at 25 °C).

In order to increase the photo-sensitive area per G-APD, a light concentrator is placed in front of each sensor. Additional advantages are the filling of the dead space due to the packaging and the shielding of photons arriving from outside the reflector surface. While for the prototype module of the camera, a simple (truncated pyramid) open geometry with reflective walls was chosen [8], the final camera was constructed using solid concentrators based on total internal reflection. Due to refraction at the surface. The achieved compression ratio can be as much as  $n^2$  higher than for hollow concentrators,  $n$  being the refractive index. The applied light concentrators have a height of 20 mm, a hexagonal entrance with a distance of the two parallel sides of 9.5 mm and a square exit of 2.8 mm  $\times$  2.8 mm. The hexagonal shape has been chosen to exploit the ideal symmetry for the trigger system and the event reconstruction. The exit area is smaller than the G-APDs to have some clearance in the positioning. The shape of the concentrator surface has been optimized by 3-dimensional ray-tracing simulations for a cut-off angle for incident photons of 22.5° [17] having a possible future extension of the reflector in mind. In the simulations a flat angular acceptance of the sensors is assumed, which is fulfilled at least up to 60° for the G-APDs employed [18]. For more details on the performance of the light concentrators, see [19].

Apart from a higher compression ratio, an additional advantage of solid concentrators is that their material and the one of the sealing window can be selected to match each other as well as the refractive index of the G-APD resin. In this way light loss due to Fresnel refractions at several surfaces can be avoided. Furthermore, mass production techniques can be applied, and also complicated shapes are available.

The applied light concentrators were produced by injection molding, using a UV-transparent polymethyl methacrylate (PMMA) granulate (PLEXIGLAS® 7N OQ, refractive index of 1.49). Together with the industrial manufacturer of the concentrators (IMOS Gubela GmbH, Renchen, Germany), the quality was successively increased until the demanding requirements regarding optical and surface properties were met. Altogether ten batches were produced, where the first four were prototypes and the last six were used for the construction of the camera. Since even for these six batches the quality was not stable enough, it was necessary to measure the spectral transmission of 2344 concentrators with a spectrophotometer and to define a cut-off criterion. As a threshold curve the lowest measured point at each wavelength for the best 25 samples were used, further subtracting 3% absolute transmission. The results of the transmission measurements are summarized in figure 9. Two main features are clearly visible for the rejected concentrators, namely an absorption shoulder between 300 nm and 380 nm and a generally low transmission for several concentrators. Both can be explained by problems during the production process, like contamination with leftovers from other (UV-absorbing) PMMA composites or changes in the cooling process. It should be noted that the measurements include the losses due to Fresnel reflections at the entrance and exit area of the concentrators (transition from air to PMMA and vice versa), which account for about two times 4%. For a camera pixel the Fresnel losses are reduced, because the refractive index of PMMA is very similar to the one of the resin on top of the G-APDs (see above).

To each of the 1535 selected G-APDs a light concentrator fulfilling the transmission requirements was glued. A two-component glue was used (EPO-TEK® 301), which has a refractive index similar to the one of the protection resin ( $\sim$ 1.5) and which is transparent down to 300 nm. The



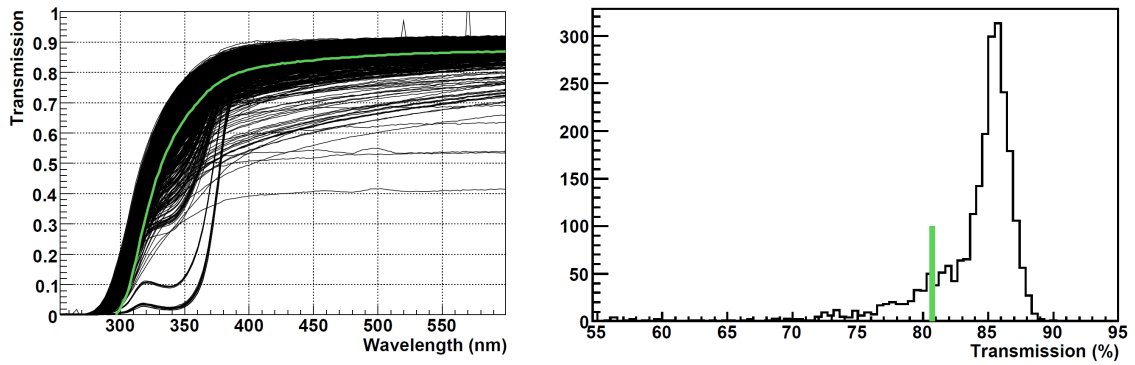


**Figure 9.** Spectral transmission of the 2344 PMMA light concentrators considered for the construction of the camera. The measurements were performed with a PerkinElmer LAMBDA 900 spectrophotometer for wavelengths between 250 nm and 600 nm in steps of 2 nm. Left: Each black line shows the result for one concentrator ( $\pm 1\%$  uncertainty). The small jumps are due to measurements errors (short exposure to ambient light during one step) and can be ignored. The green curve represents the cut-off which was used to reject concentrators of poor quality. Right: Projection of the measurement results for a wavelength of 400 nm (zoomed, cut-off line in green). The measurements include Fresnel reflection at both, entrance and exit surface.

glue was first placed on the concentrators with a high precision dispenser, and the concentrators then attached to the G-APDs using custom-made alignment tools (see figure 10, left). Afterwards, both, a load test and a functionality test were performed. During the load test the pixels were fixed on the G-APD side (in horizontal position) and a 200 g weight was put on the opposite side on the concentrator.

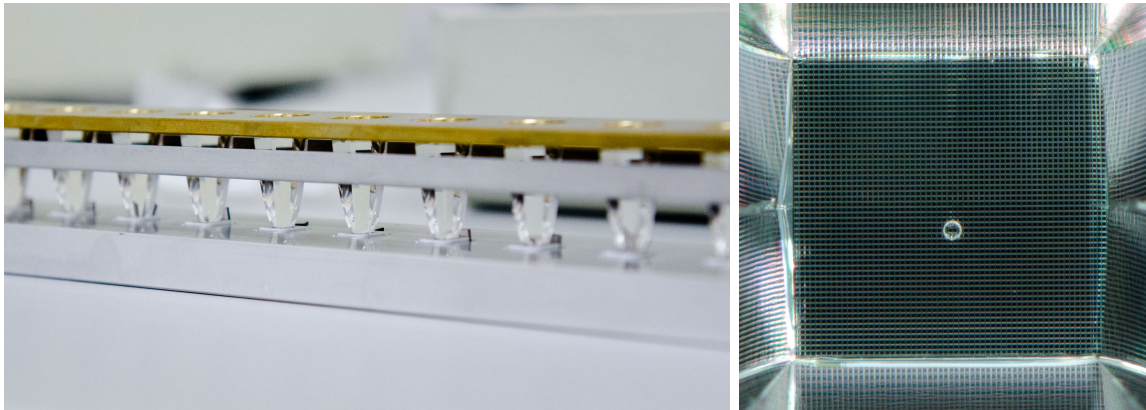


**Figure 10.** Left: Photograph of the alignment tool to glue the light concentrators onto the G-APDs. The sensors are fixed in custom-fit sinkholes on the bottom (white ceramics packaging visible), while the concentrators are positioned with two horizontal metal bars. Right: One of the pictures taken per pixel for quality control. The 3600 G-APD cells are visible and also part of the concentrator walls. The bright spots at the borders are due to reflections. In the middle, an air bubble can be seen, affecting 16 cells. Since this is just 0.4% of the total area, this pixel was accepted. Also it should be noted that only a fraction of the photons hitting the bubble really get lost.

For the functionality test, the G-APDs were supplied with their nominal voltage and illuminated with a nano-second light source at a wavelength of 450 nm to check for a signal. While two pixels failed the load test, none of the remaining ones failed the functionality test. In addition, a high-resolution picture of the sensor area as seen through the concentrator was taken with a macro-lens (105 mm focal length; see figure 10, right). In this way glueings of poor quality, e.g. with many or large air bubbles, could be spotted. Inspecting these pictures, 24 more pixels were rejected. Thus 1509 pixels were available for the camera construction.

In the next assembly step, 1440 pixels were glued to the camera window which is optically identical to the concentrators. For the glueing the concentrators were placed face down on the window, and the glue (Acrifix<sup>®</sup> 1R 9019 Solar) was injected at the side (see figure 11, left). After some unsatisfying first attempts the manufacturer (Röhme Evonik GmbH, Darmstadt, Germany) was consulted and some Acrifix<sup>®</sup> 1R 9016 Solar was admixed. This avoided air bubbles because the glue was sucked in more homogeneously by capillary forces.

Since four or five G-APDs share the same voltage supply channel (c.f. section 2), the pixels were sorted before being glued to the window. The resulting spread in breakdown voltage is  $\leq 10$  mV for 94% of the 320 groups and the remaining 6% were mounted at the border of the camera. In order to avoid cable tensions on the G-APDs, small Printed Circuit Boards (PCB) were soldered to their back side (see figure 11, right). The co-axial cables for the bias voltage and the signal transmission are connected to these PCBs (one cable per sensor, nine sensors per PCB). Figure 12 shows a photo of the fully assembled sensor compartment (without cover). The PMMA window is fixed to an aluminum flange to which also several distance pieces are attached. These bars support the insulation plate introduced in section 4.1, which includes boards for electrical connections. While the co-axial cables coming from the G-APDs are plugged at one side of the connector boards, on the other side (in the electronics compartment) plug-connections for the signals and the bias voltage are provided. Each connector board serves a group of nine pixels, thus two voltage and nine signal channels. In this way the sensor compartment can be de-attached from the rest of the camera. To monitor the conditions near the G-APDs, 31 temperature and two humidity sensors have been installed (IST P1K0.520.4W.x.010 and Honeywell HIH-4031-0015, respectively).

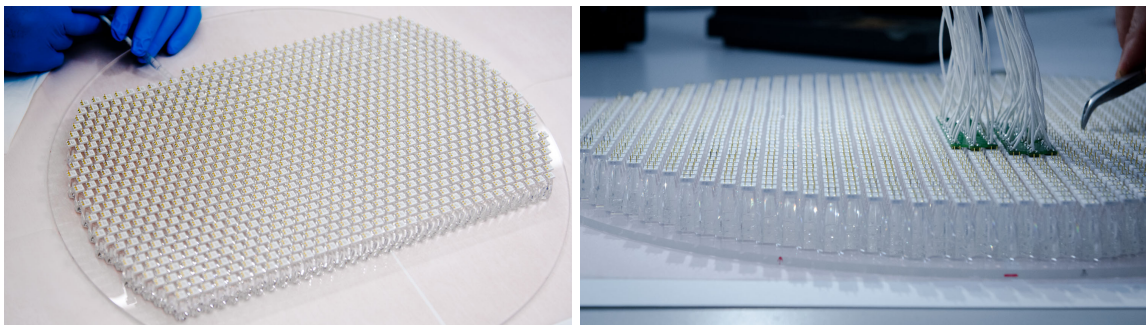


**Figure 11.** Photographs documenting two work steps during the assembly of the sensor compartment. Left: Glueing of the pixels onto the camera window. Right: Soldering of the PCBs for the signal and bias-voltage connection on the G-APD contacts (facing upwards).

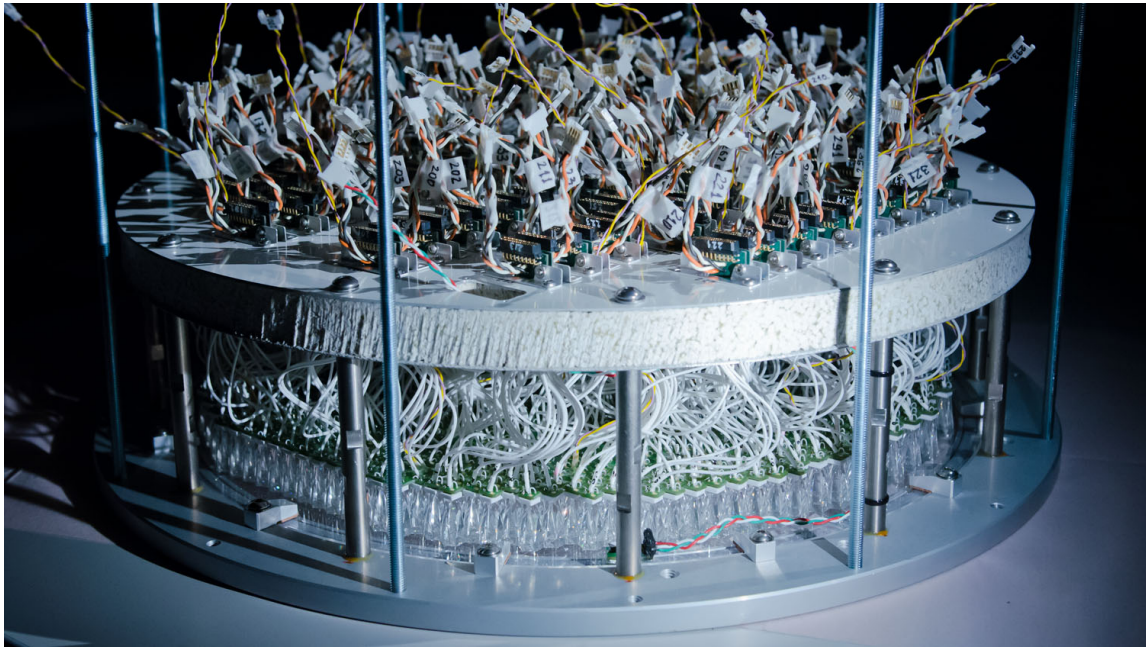


**Figure 12.** The assembled sensor compartment. From bottom to top the front flange with the entrance window, the light concentrators, the G-APDs (white packaging), the PCBs (green) for the co-axial cables (white), and the insulation plate can be seen. The black connectors on top are for the G-APD signals, the three-pole cables (white-black-orange) for the bias supply. Other colored cables (yellow-purple and red-green-white) connect the temperature and humidity sensors. For the final mounting the sensor compartment is protected by a cover (replacing the thread bars).

### 4.3 Readout and Trigger Electronics

The analog signals from the sensor compartment are processed and digitized inside the camera by means of custom-made electronics boards. One pixel corresponds to one readout channel, thus in total there are 1440 channels. Most of the electronics is realized on 40 board pairs, which are mechanically integrated in four crates as introduced in section 4.1. Each pair consists of a preamplifier and a digitizer board and serves 36 channels. The two PCBs of a pair are connected via one midplane per crate, which carries in addition supply voltages and RS 485 communication lines. Figure 13 shows a photograph of the midplane. In order to initiate the digitization and the transfer of the event data, the digitizer boards receive a logical signal provided and distributed by the trigger system. For an overview, see also [20].

#### 4.3.1 Preamplifier and Trigger Signal Conditioning

The preamplifier board features 36 channels grouped in four patches reflecting the structure of the trigger system and the digitizer boards. Its first stage is a grounded-base circuit (npn transistor, BFR 182) with an input impedance of  $25 \Omega$ . At the collector resistance ( $200 \Omega$ ) the sensor current is converted into a voltage, which is further amplified (OPA 3691, Texas Instruments) giving after line matching a conversion gain of  $0.45 \text{ mV}/\mu\text{A}$  at about 200 MHz bandwidth. This corresponds to a single-avalanche amplitude of 2.25 mV at the  $50 \Omega$  input of the digitizer board. For trigger conditioning, the preamplifier signal is used as well. First a linear addition of the signals from one



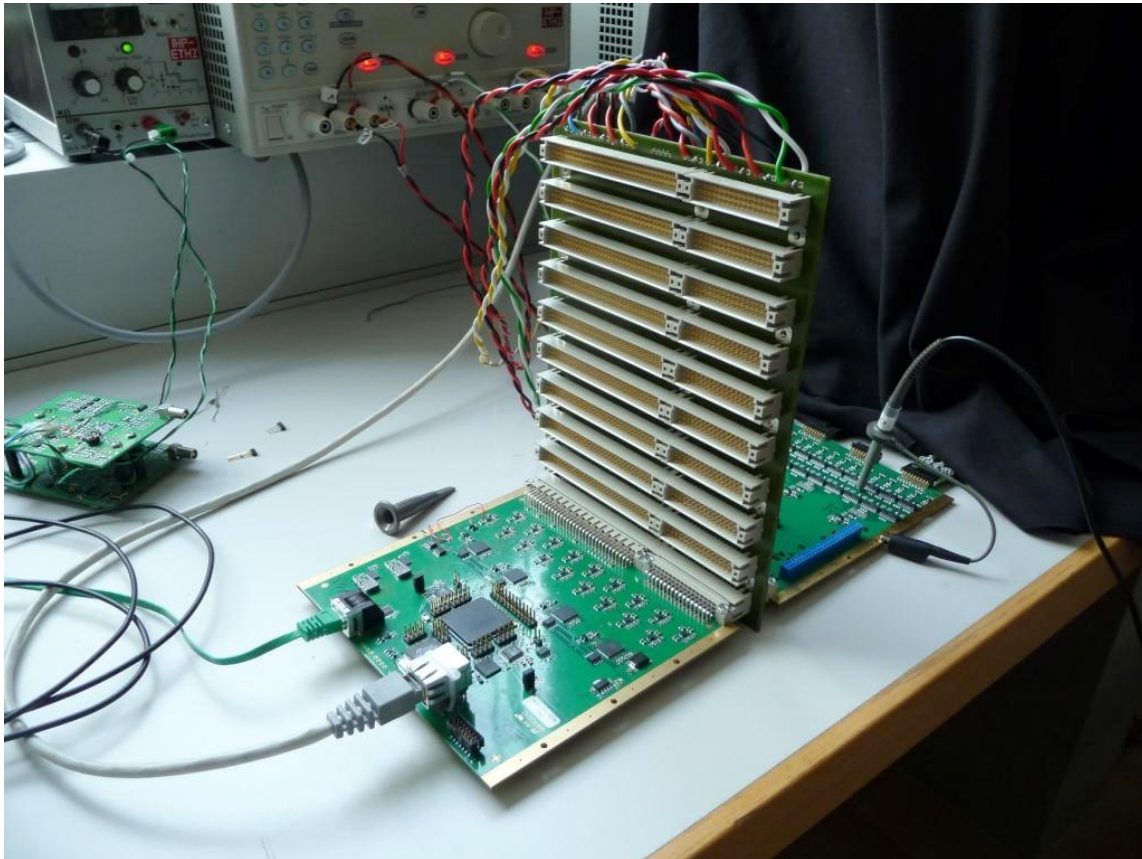


**Figure 13.** Laboratory setup with the midplane of the electronics crates and one preamplifier board (right) and one digitizer board (left) plugged in the first slot. On the top, temporary cables for low-voltage supply and slow-control communication are connected.

patch is performed (OPA 691, Texas Instruments), with the possibility to exclude individual pixels (e.g. due to noise). Cable-based clipping is used to shorten the length of the 9-fold sum signals to 10 ns before they are fed into a comparator (LMH 7220, National Semiconductor). At the input of the comparator an avalanche is represented by a voltage of 9 mV. The comparator signal from each of the four patches is sent to a trigger unit realized as a mezzanine card on the preamplifier board. This unit provides also individual pixel disable signals and the comparator thresholds.

### 4.3.2 Trigger Unit

The trigger unit is equipped with an on-board field-programmable gate array (FPGA, XILINX Spartan-3AN family, XC3S400AN-4FGG400C). It controls an 8-channel digital-to-analog converter (DAC, LTC 2620) with a resolution of 12 bit and a full range of 2.5 V (270 photon equivalents) to set the comparator thresholds (15 DAC counts/p.e.) provided to the preamplifier board. The four comparator output signals from the latter are summed at a time, and the summed signal serves as input for an N-out-of-4 logic. The threshold level  $N$  is defined by a discriminator, whose threshold is also provided by one of the FPGA controlled DACs. During standard physics operation, the N-out-of-4 logic is operated as 1-out-of-4. Since this discriminator logic requires a minimum length of the signal of the order of several nanoseconds, by design, the second trigger

stage acts as a filter on electronics noise. The digital output signals of all 40 trigger units are sent via coaxial cable to the trigger master board making the final decision and distributing the trigger signal to the digitizer boards. To monitor the rate of all trigger channels, a counter for all comparator and discriminator outputs is implemented. This is essential in order to adapt the threshold for single more noisy channels due to e.g. bright stars in the field-of-view during operation. The counter readings as well as the command values for the setup of the trigger unit are transmitted to/from the trigger master board via an RS 485 serial connection.

### 4.3.3 Trigger Master Board

The main purpose of the trigger master board is to generate the final trigger signal based on the input from the 40 trigger units, and to provide a common reference clock for all sampling chips on the digitizer boards. Its core component is an FPGA (Xilinx Spartan-3 family, XC3SD3400A-4FGG676C) controlling all sub-components and providing a 100 Mbit Ethernet connection to the counting house through a Wiznet W 5300 chip. A trigger decision is taken when  $N$  out of the 40 primitives have a rising edge within a time-window adjustable from 8 ns to 68 ns in steps of 4 ns. During physics data-taking this majority coincidence is operated with  $N = 1$  and the window is set to 12 ns. It is avoided to process the trigger signals in the FPGA on the trigger units to keep their individual jitters as small as possible. The jitter on the trigger output from the trigger master board FPGA is a few nanoseconds and can be neglected for the global readout time.

In addition to the physics triggers, the trigger master board can generate pseudo-random triggers, as well as triggers for the internal and external light-pulsers with a rate between 1 Hz and 1 kHz. After sending a trigger to one of the light-pulsers, the multiplicity  $N$  is changed for a short time-interval to e.g. 25 to avoid interference with physics triggers. Furthermore, two external trigger inputs and a veto input are available. All trigger outputs can be switched on and off individually such that, for example, random and light-pulsers events can be interleaved during data-taking.

After a customizable delay, a rectangular signal, called time-marker, is created and distributed to all digitizer boards where it is mixed into one channel of each sampling chip. Having the delay adjusted such that this marker is sampled at the end of the readout window, it serves as cross-check for individual delays between boards and chips. After a second adaptable delay, the trigger decision is propagated as logic signal to the data-acquisition boards to stop the analog ring-buffers continuously sampling the data for readout. Both delays are implemented in the FPGA. During digitization, and until sampling is restarted, the data acquisition boards emit a busy signal preventing further triggers during that time.

Just after a trigger decision, a bit pattern containing a trigger counter and the source which generated the trigger is sent via a serial RS 485 bus, one per crate, to the data acquisition boards. There it is included in the raw data stream. A custom dead-time is set, to ensure new triggers are rejected until the transfer is complete. The trigger counter is stored and can be readout via Ethernet together with counters for the total run-time and on-time. The latter takes into account the busy-time of the DAQ boards, the dead-time and also the time to wait for light-pulsers triggers. It thus measures the overall time when the camera is ready to accept triggers.

Additionally to the trigger signal, the trigger master board provides the reference clock for the digitizer boards as  $1/2048$ th of the sampling rate. In order to generate this signal with a jitter below 100 ps, a clock conditioner (National Semiconductor LMK 03000) is used. This device also

provides the possibility to change the sampling rate within certain limits. A second output of the clock conditioner is used to generate a square signal, which can be distributed as substitution of the time-marker to calibrate the timing behavior of the analog pipeline chips on the digitizer boards. In order to distribute the fast signals (trigger, reference clock and time marker) the LVDS standard and slim Wirewin Cat.6 cables with RJ-45 connectors are used. Two dedicated distribution boards were designed for this purpose. They comprise two ten-fold fan-outs (ON Semiconductor MC100LVEP111) for every signal, and introduce only a low jitter ( $< 20$  ps) and skew ( $< 250$  ps). Auxiliary input and output signals are distributed as NIM (Nuclear Instrumentation Module) logic levels. The configuration of all 40 trigger units is done through the trigger master board and communicated via a dedicated RS 485 bus.

#### 4.3.4 Digitization

The digitization of the 1440 G-APD signals is done on 40 boards, each comprising  $4 \times 9$  channels. These digitizer boards have five important parts: input buffers, analog pipeline chips, analog-to-digital converters (ADC), an FPGA, and an Ethernet chip. At the input buffers the single-ended preamplifier signals are converted to differential ones using fully differential amplifiers (ADA 4950, Analog Devices) set to a gain of two at a bandwidth of 300 MHz. This chip allows also to feed in signals for timing calibrations, DC levels for amplitude calibrations, and an adjustable common-mode voltage. The latter shifts the signals into the optimal range for the pipeline chips having a dynamic range of about 1 V.

Sampling of signals is based on the Domino Ring Sampler (DRS 4) chip, developed at the Paul Scherrer Institute [21]. Each chip comprises  $9 \times 1024$  capacitors and samples continuously the nine input voltages. The values are stored in pipelines until a trigger stops the sampling. Any number of samples can then be digitized. The system can be operated with a sampling frequency of 0.7 GHz – 6 GHz. During standard data taking 2 GHz are used and 300 values (150 ns) are read out. In this way also large signals from the light pulsers are completely contained in the readout window. During calibration measurements, necessary to calibrate the properties of the capacitors of the DRS 4, all 1024 samples are digitized. In order to calibrate the gain of each capacitor, a voltage level is fed into the DRS 4 input via the differential amplifier. This voltage is produced by a 16 bit digital-to-analog converter (DAC, LTC 2600, Linear Technology). For more details on the DRS calibration, see [21] and references therein.

All 160 DRS 4 chips employed in the electronics are locked using their internal phase-locked loop to a common frequency generated by the trigger master board. In this way, a precise relative timing between all channels of about 300 ps is possible [21] (depending on the sampling frequency), provided that the fixed-aperture jitter of the DRS 4 is calibrated. This timing calibration is performed by using a 250 MHz clock signal, generated by the trigger master board. For dedicated runs, this signal can be capacitively coupled into channel nine of each DRS 4 chip. Alternatively, a high-precision time marker, also generated by the master board, can be imprinted on the analog signal of every ninth channel. In this context, it serves as cross-check for the timing calibration.

Following a trigger, 12 bit analog-to-digital conversion (AD 9238, Analog Devices) at 20 MHz is started. The differential outputs of the DRS 4 have a gain of two, thus allowing in principle for a dynamic range of 2 V at the ADCs. However, the dynamic range is reduced to 1.8 V by an intended baseline shift and a compensation for individual DRS 4 offsets. All digital settings are controlled



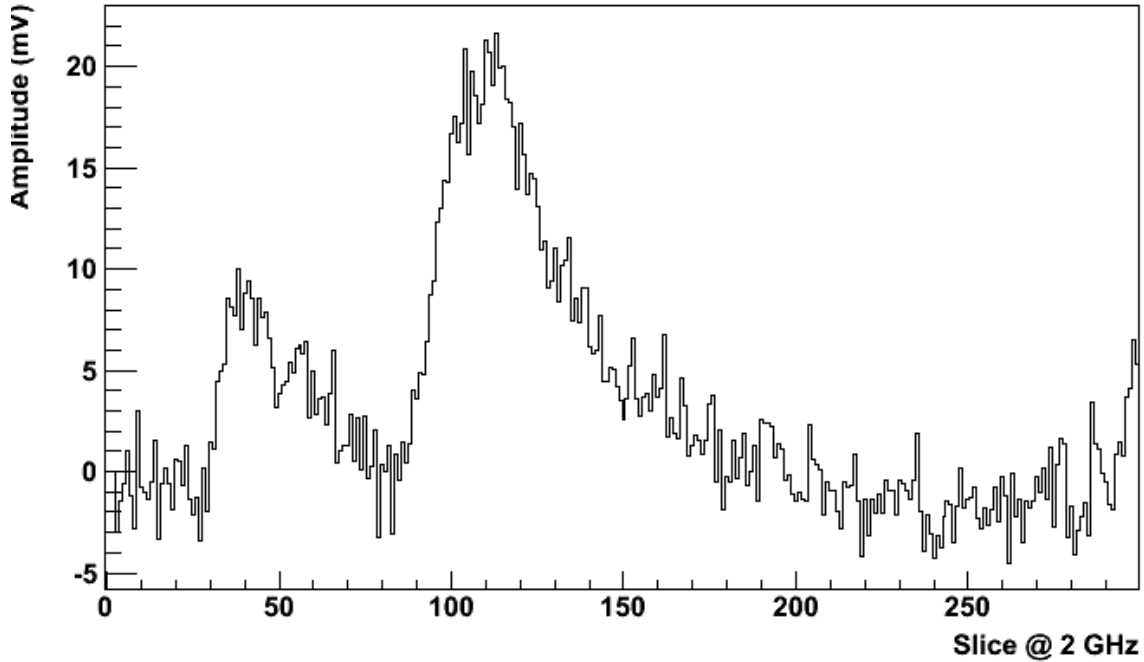


**Figure 14.** Example of an event as recorded by one readout channel. The data were taken with closed shutter and using a random trigger. A single and a double-avalanche signal are visible. On the x-axis the sample position within the DRS 4 pipeline (sample number after trigger) is given in steps of 0.5 ns. On the y-axis the amplitude is shown (1800 mV full scale).

by an FPGA (Xilinx Spartan-3 family, XC3SD3400A-4FGG676C), i.e. the sampling mode, the serial conversion mode, the calibration options, and the DAC values. Another important task of the FPGA is to organize the communication and data sending. Each digitizer board has an Ethernet interface (Wiznet W 5300 chip) implemented for this purpose.

Figure 14 illustrates the performance achieved with the readout electronics. Shown is one frame, i.e. 150 ns, of a single channel recorded with the corresponding G-APD on nominal voltage and the shutter of the camera closed. A random trigger has been used for data taking. The DRS calibrations have been calculated using calibration runs taken shortly before the data run and have been applied offline to the data. Two signals due to dark counts are visible, where the double-avalanche is probably due to optical cross-talk within the photo sensor. While the noise level is about 2 mV root-mean-square, the peak amplitude per avalanche is about 10 mV. The total gain of the signal chain is 1.8 mV/ $\mu$ A.

## 4.4 Power, Cooling and Auxiliary Systems

### 4.4.1 Power Conversion and Distribution

Three-phase AC power is received from the MAGIC [9] power lines. A 3-phase filter followed by a main choke provides power to the drive cabinet. In parallel to the drive, the three phases are filtered individually, separately serving the computer infrastructure, the camera and the cooling system. The camera uses three Agilent AC-DC supplies, one for the G-APD bias supply (NS 5769A) providing 85 V, another one for the interlock system and the heaters providing 24 V, and the main

supply (NS 8737A) for all camera systems providing 48 V at about 12 A. Two 45 m long cables bring the power to the patch panel (backplane) of the camera. Inside the camera DC-DC converters (VICOR VI-J300 series) are used for power conditioning. The output of each converter is equipped with an adapted filter, mainly a common mode choke and a low ESR Tantalum capacitor, which is mandatory in order to achieve the required noise levels. In addition, step-down converters are used on the digitizer boards (c.f. section 4.3.4).

All output voltages and currents are monitored continuously using shunt resistors. For this purpose the corresponding analog signals are routed to a slow control board (see section 4.4.5) where they are digitized and transmitted to the counting hut. The camera houses four DC-DC converter boards, each serving one of the DAQ crates and two additional DC-DC converter boards supplying all remaining power consumers, namely the trigger master board, the two fast signal distribution boards, the internal and external light-pulsers, the slow control board, and the two Ethernet switches.

The total power consumption of the camera electronics during operation is about 570 W. About 100 W are dissipated in the supply lines and another 100 W due to the limited efficiency of the DC-DC converters, yielding a total of 370 W consumed by the electronics. An additional 100 W are used by the G-APD bias supply systems. During powering up the FPGAs on the digitizer boards and on the trigger units, significant extra power is needed. The resulting load would exceed the limits of the DC-DC converters (and eventually of the power supply). Consequently, the digitizer boards in each crate are inter-connected such that they boot sequentially, one after the other.

#### **4.4.2 Bias Voltage Supply**

The bias supply system provides up to 416 DC voltage channels, each programmable between 5 V and 90 V with 12 bit resolution ( $\sim 20$  mV step width). Currents of up to 4 mA per channel can be supplied and measured with 12 bit resolution. In practice 1% precision is achievable due to regulation noise. Each channel has an over-current protection circuit, disabling that channel at the limit of 4 mA until a reset command is received. The complete system is built as a double-height VME-like crate with slots for 14 subunits. While one slot is occupied by a controller, up to 13 motherboards with 32 voltage channels each can be plugged. All units are forced-air cooled. For the operation of the sensors 320 voltages channels (ten motherboards) are needed. In figure 15 a photograph of the crate is presented.

A single external voltage supply providing up to 100 V is employed (Agilent N 5769A) from which the output of each channel is derived. Usually a voltage limit of 85 V is set for this unit. Each channel is realized as a plug-in card to a motherboard. A high voltage, high current operational amplifier (OPA 454, Texas Instruments) with internal over-temperature and over-current protection is used, controlled by a 12 bit digital-to-analogue converter (DAC). Precise calibration of the output voltage requires adjusting a potentiometer while measuring the voltage from each card. The motherboards employ a Programmable Logic Device (PLD) to communicate with the controller, the DAC and the ADC chip. Also the controller is based on a PLD and communicates based on a three-byte protocol via a USB connection with the control computer. The USB connection is based on an FTDI chip (FT 245R). The interface protocol allows channel-wise voltage setting, reading of the currents and the over-current protection status. Ramping is needed, since an immediate application of the operational voltage would trigger the over-current protection due to the large load capacitance and initial current of the G-APDs. A continuously increasing 3 bit counter is sent with

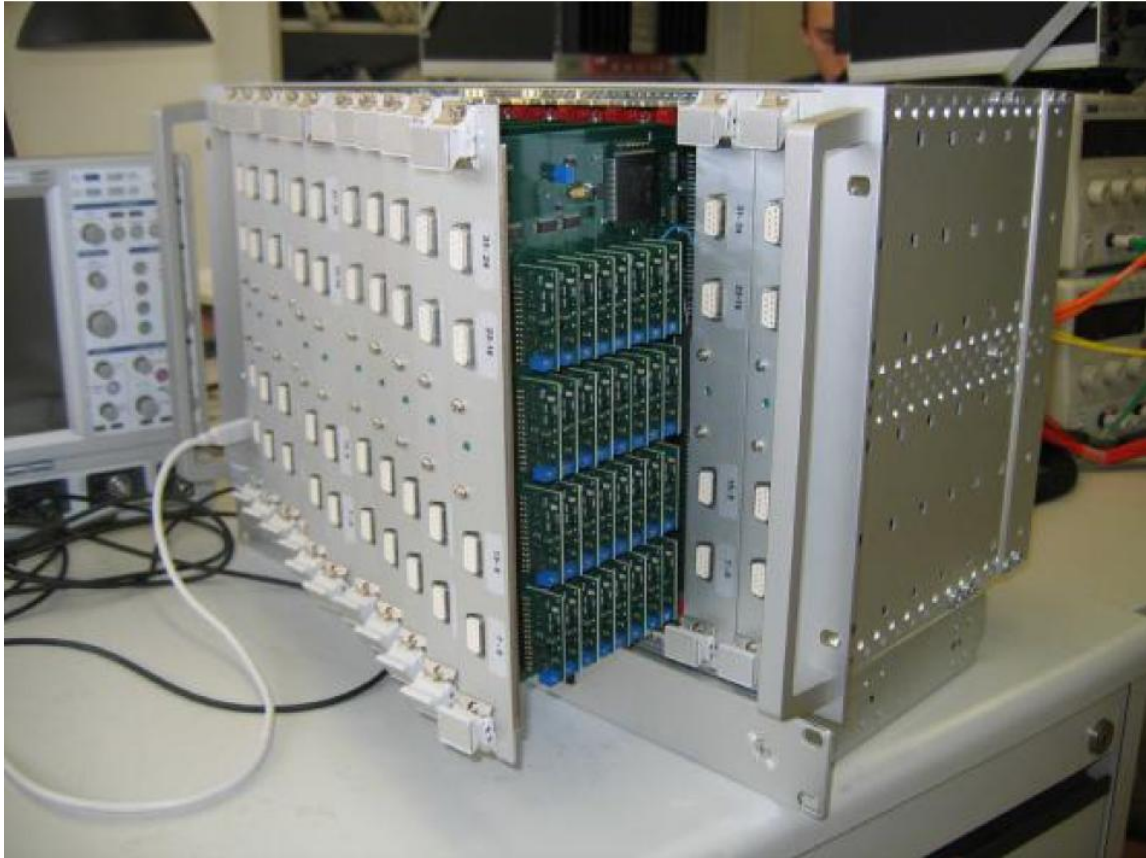


**Figure 15.** The bias-voltage crate supplying the G-APDs. On the left, where the USB cable is plugged, the controller is located. For this photograph most of the motherboards have been pulled out. On the board in the front the 32 plug-in cards, each constituting one channel, are visible.

every data transfer from the system controller to allow for integrity checks. The cycle time for one command is about  $50 \mu\text{s}$ . Over USB this speed is achievable only by using bulk transfer of several commands.

#### **4.4.3 Interlock System, Remote Control and Heaters**

Since summer 2012, the telescope is regularly operated remotely, i.e. without a person present in the FACT counting hut. In order to allow this, remote control is required and an interlock system was installed to secure the unattended operation. The interlock system gets input from the cooling unit (see section 4.4.5), the fan status of the G-APD bias system and remote commands transmitted via an Arduino micro-controller. It controls the 48 V main supply, the power for the G-APD bias system and also the main AC lines for the drive cabinet. Status information is provided locally by LEDs and by the Arduino interface for remote access. The system operates as follows:

1. The 24 V supply for the interlock system must be switched on, otherwise all other systems are blocked. This supply cannot be controlled remotely.
2. A button to overwrite the locked status has to be hold for some seconds, while the Pump-start button is pushed. This will turn on the pump of the cooling system and lead to correct

readings of the flow and pressure status signal from the cooling unit. At this moment the overwrite button is no longer required and the system will self-hold the on-condition as long as pressure and flow are sufficient.

3. This enables the main camera supply as well as providing 230 V to the fan tray of the G-APD bias supply. The feedback from this fan-tray is used to enable the Agilent for the G-APD bias system as well as providing 230 V to the G-APD bias crate.
4. Pressing the Stop button will interrupt the self-hold circuit and turn off the pump. At the same time all other devices are disabled and powered down.
5. In case of a cooling failure the system behaves in the same way as if the Stop button was pushed (see point 5).
6. The drive cabinet can be powered up and down independently by remote commanding.

All above mentioned buttons can be activated remotely in the same way, using the Arduino interface, including the read-back of the status information. Moreover the interface allows the commanding of power relays controlling the 3-phase main input lines to the drive cabinet.

The camera features a set of eight ohmic heaters, each providing 40 W at 24 V. Two of them are installed per crate. They are controlled by two thermo-switches, closing at 4 °C and opening at 13 °C, built into the camera. This system uses the 24 V from the interlock supply and thus is always enabled. Remote control is extended to the AC power for all FACT computers using power sockets with Ethernet interface.

#### **4.4.4 Cooling System**

The Hamamatsu MPPCs used as photosensors have a gain variation of  $\sim 5\%/K$ . They are glued onto the light concentrators, which are in turn glued to the front window (c.f. section 4.2). It was desired to limit the temperature variation across the sensor plane to 0.1 K/cm and to a maximum difference of 2 K between any two sensors. A specific operation temperature is not required. Since the electronics inside the camera dissipates about 570 W, an active cooling system is required to prevent overheating of the components. In order to study the thermal behavior of the camera, a thermal model of a quarter of the camera was created by a specialized company (Thermotech division of AMS Technologies), and the results were used to optimize the design.

The camera is thermally divided into two compartments by means of a baffle plate. The sensor compartment has no active cooling system. The electronics compartment is water cooled. A central cooling plate carries the four electronics crates and the supports for the DC-DC converters. The water flows consecutively through the central plate and the crates. Electronics boards are designed with heat spreading planes and attached to the crates using CALMARK wedge-locks. The extra boards (trigger master, slow control and fast signal distribution) are thermally connected to the outside of the crates. The custom cooling unit is IP55 compliant. It is located at the telescopes rotating platform inserted into a second casing protecting it from splash water. It provides a flow of 6.8 l/min at a maximum pressure of 5 bar. A heat exchanger cools the water, containing an anti-freeze (Glysantin<sup>®</sup> G48<sup>®</sup>), to ambient air temperature. About 10 m long water hoses connect to the camera. Switches reacting on a too low water flow or pressure deliver an enable signal to the interlock system. Without a running cooling system the camera is non-operable (see section 4.4.3).

#### 4.4.5 Slow Control Board

Inside the camera the temperature, the humidity and all supply voltages are monitored continuously. A dedicated slow control board was developed. It features an Atmel ATmega32L micro-controller and a Wiznet W5300 Ethernet interface for data transmission. A total of 148 channels can be multiplexed onto a 24 bit ADC, AD7719, with integrated current sourcing for temperature probes. Concerning temperature and humidity, the slow control board reads out:

- 31 temperatures close to the G-APDs in the sensor plane
- 2 temperatures per readout crate, 8 in total
- 2 temperatures per DC-DC converter board, 12 in total
- 4 temperatures at the camera patch panel close to the cooling connections
- 4 times the humidity, once close to each crate

As temperature sensors, PT 1000 are used.

#### 4.4.6 Shutter

The camera features a remote controllable shutter. Two linear actuators of type LA 23 (LINAK AG, Thalwil, Switzerland) operate independently the two shutter panels. The motors are controlled using an Arduino microcontroller hosting a dual Pololu VNH-5019 motor driver board. The system controls the power status of the motors, sets the motor speed and drives the motors by providing power. It reads the motor currents and the integrated hall sensors providing the motor positions. The system is completed by an amplifier and filter card, for noise reduction on the hall sensor reading and in order to obtain a second low current measurement. An additional 24 V low voltage supply is used to power the system. Communication with the Arduino is established via Ethernet, and a USB interface is available for debugging and firmware upgrades. The system is operated independently of all other systems.

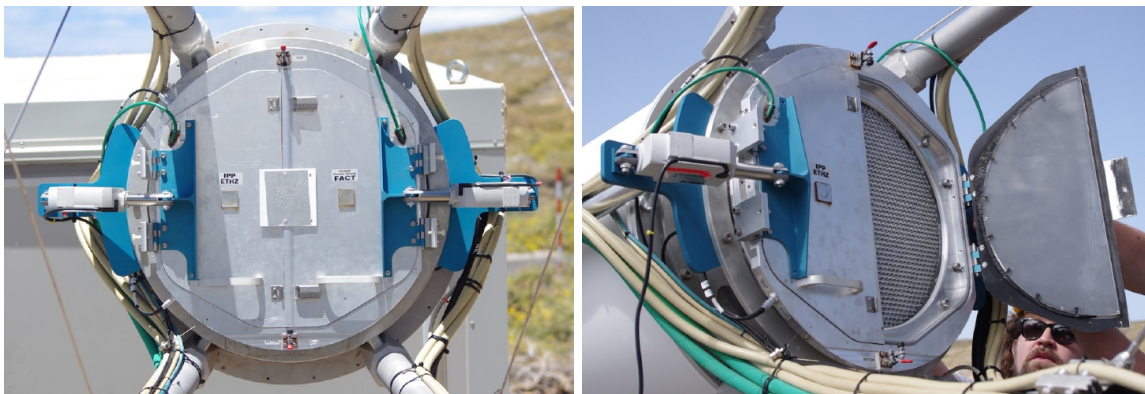


**Figure 16.** Photographs of the installed camera showing the shutter installation. Left: Closed shutter situation. The green cables visible on the top part of the picture provide power and control for the internal light pulser system. The square plate in the center of the camera shutter is used as a screen, when pictures of star reflections are taken for the pointing calibration. Right: Situation with one half of the shutter opened. On the inner side of the opened half, the internal light pulser plate can be seen.



## **5. Online Software and Data Storage**

### **5.1 Overview**

The slow control and data acquisition system is based on C++11 and implemented under recent Linux using several available standard libraries. Its source code is open and stored in a svn repository. As build system, GNU autoconf and GNU automake is employed. The C++ boost libraries [22] are used as C++ extension.

The system is currently installed on the latest Long-term Support version of Ubuntu (12.04 LTS). All libraries in use, except CERN developments, are available from their repositories. For global authentication an LDAP server is in use. As database backend a MySQL 5 server is employed. Web-pages are served by an Apache 2 web-server with php 5. The whole system is composed by several machines monitored by the Munin monitoring system [23]. The system is reachable from the outside as a Virtual Private Network (vpn).

A general overview of the implementation is sketched in figure 17. The control system is split into several programs, each responsible for a single task. This keeps algorithms logically separated ensuring easy maintenance on the long run. Each program internally implements an event driven state machine. All communication is decoupled from the state machine providing non-blocking behavior. Processing of all events is synchronous ensuring robust operation and avoiding any possible race conditions from the very first. Events can originate from the inter-communication of programs, data received from the hardware or the built-in console interface. Inter-communication is implemented through CERN's Distributed Information Management System (DIM, [24]). The hardware communication via Ethernet and USB is managed by the asynchronous I/O library (ASIO). The readline-based console interface features a history and tab-completion.

### **5.2 Sub-components**

#### **5.2.1 System Configuration**

Each program retrieves its configuration automatically from different sources, each with a different priority. The main sources are local resource files and a configuration database. While the local files feature mainly an easy way to alter the configuration for debugging purposes, the database is used during operation. The database is editable through a custom made php-based web-interface. Whenever the database is altered, the history of changes is kept being able to reconstruct the complete setup during any previous data-taking. Configurations from two different times can easily be compared through the web-interface.

#### **5.2.2 Inter-communication**

The communication between the programs implemented via DIM is organized in a server-client setup. Every server is registered at a central name-server allowing the access from any client by name. Servers offer named commands and data services. After subscription of a client to a data service, new data is distributed automatically to all subscribed clients. Received commands and service updates are both queued in an event queue of the state machine and processed synchronously in the event loop.



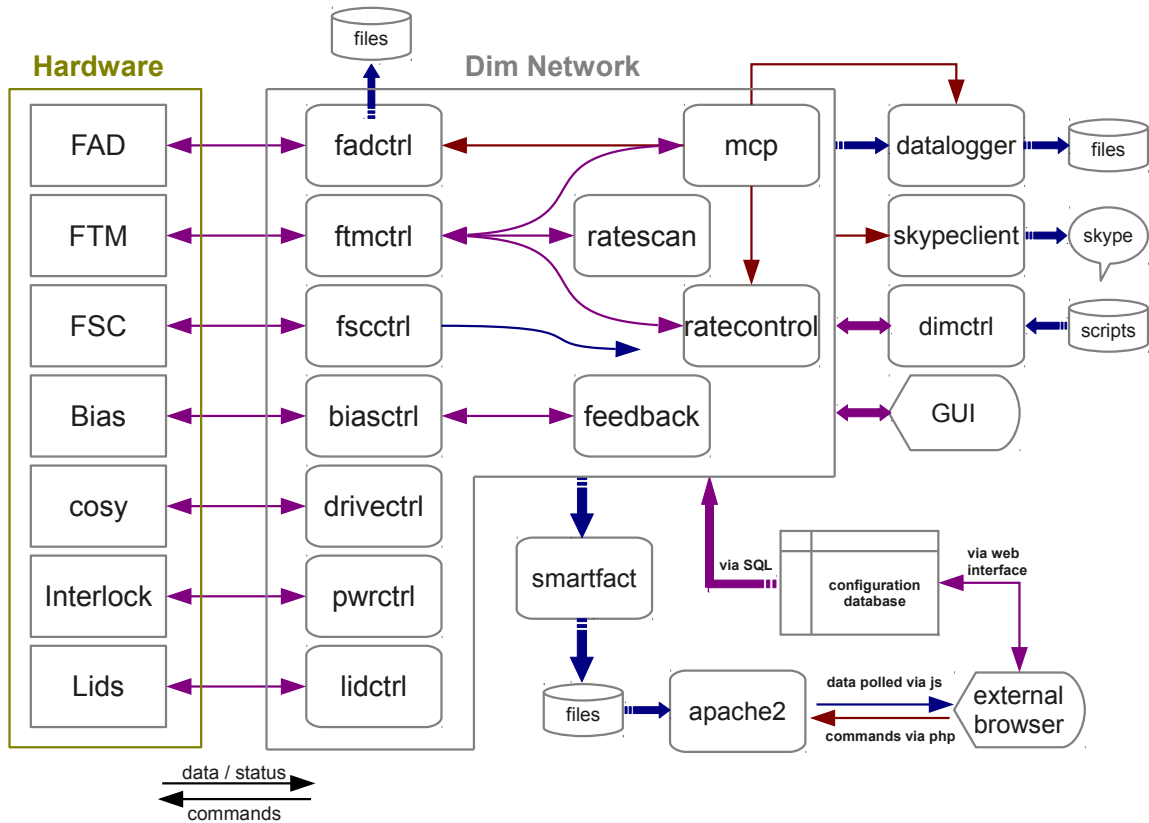


**Figure 17.** Schematics of the slow control system. Only the most relevant paths for data-exchange are shown. Magenta denotes command and data-paths, red the direction of commands and blue the direction of data-flow. The abbreviations denote the following components: FAD (digitizer boards), FTM (trigger master board), FSC (slow control board), Bias (bias voltage supply), cosy (drive system). Other abbreviations are explained in the text.

The DIM network has been enhanced with a special service distributing command and service descriptions of each program. These descriptions allow to display help texts for commands and their arguments, and name the elements of each service. Named elements allow a central data collector to automatically subscribe to all services and write the transmitted data to files. The files then contain a full description of the data stored, and each change to the data services is transparently logged.

### 5.2.3 Data Storage

All slow control data and logging output is collected by a central *datalogger*. For each service, a file is kept open in FITS format [25]. Every day at noon, a new file is opened. Since several special features are needed in this context, like updating the headers during streaming, the FITS output is based on the cfitsio-library and its C++ wrapper CCfits [26]. Files in FITS format contain a complete description of the data stored. This description is automatically constituted from the format description available for each DIM services and the custom element description offered by each server. The FITS format was chosen because it features self-contained data by storing a full

format description in the header. It is easy to implement, widely spread in astronomy and several tools and libraries are available.

The raw data received from the data acquisition hardware is preprocessed by the event-builder, both described in more details in section 5.3, and also stored in FITS format. The simplicity of the format allows sustained streaming of the data implemented in a custom FITS streamer class. A complementary class for reading the data as a continuous stream is also available. Advantages of a custom implementation are the absence of any non-essential feature slowing down the streaming process and the possibility to compress and decompress data streams during reading and writing on the fly using the zlib-library [27]. The FITS CHECKSUM [28], a simple integrity check, is calculated and checked on the fly whenever a file is written or read.

#### 5.2.4 Dimctrl

As a central DIM client, a program called *dimctrl* is available. Although each program can be accessed individually from its console interface, *dimctrl* features a central command interface. Loading batch scripts from file allows to automate simple processes. In addition, a JavaScript (ECMA script) interpreter is available, implemented by means of Google's JavaScript engine V8 [29], which allows full access to the DIM network and access to the database. Running JavaScripts decoupled from the DIM network in a sandbox allows to stop them at any time. This allows to recover a hanging system in case of an unforeseen event without the need to terminate *dimctrl*. By this, no log-in to the local machines is required anymore. Database access allows to directly retrieve and execute the observation schedule, provided by an automatic scheduling program or interactively by the user.

#### 5.2.5 Graphical User Interface

The graphical user interface (GUI) is implemented using Qt 4 and the qt-designer [30]. CERN's root [31] is used to display histograms and graphs, and a two-dimensional camera display is drawn through an OpenGL [32] context. It is the only program implementing its own Qt 4-based event loop not offering itself as server, thus not being able to receive commands from any client. The GUI subscribes to all DIM services of interest and posts their updates to the Qt 4 event loop from where the corresponding GUI elements are altered accordingly. User events are directly emitted as DIM commands to the corresponding servers.

The advantage is the complete decoupling of the graphical interface from the control system, thus the decoupling of a part known to be a primary source of problems during data-taking. The drawback of the GUI connected to the DIM network is the missing tolerance of the DIM network against slow network connections or blocking handlers used to process the incoming data. Consequently, a slow network connection and the transmission of large data as service update or command can block all DIM clients at once. This makes the GUI only an option for local control or to be exported indirectly, e.g. via a vnc connection. A central DIM engine could buffer all service updates and selectively distribute those data to other clients, taking into account connection speed. However, this would require additional development work.

## 5.2.6 Smartfact

For a stable remote operation of the telescope, a complete decoupling of the interactive user-interface from the control system is necessary. This is done keeping all communication within the DIM network locally and implementing external communicating with the user through a web-server.

The Smartfact user-interface, as shown in figure 18, is based on a small JavaScript. The JavaScript is once retrieved from the web server. To load a page, the JavaScript reloads a small description file from the server. From this description, the displayed HTML is constructed dynamically. The displayed data is reloaded every few seconds from the server. Both, structure-files and data-files, contain only the relevant information in a compressed format to keep the network traffic below 1 kB/s. This allows to control the system even over extremely slow connections. The displayed graphics is rendered using canvas-elements defined in HTML 5.

The back-end of the Smartfact interface is the *smartfact* program subscribing to all services of interest. Either triggered by the reception of a service update or in regular intervals, the data-files on disk are updated. For simple astrometric calculations, e.g. an overview of the zenith angle of all possible sources over the whole night, *libnova* [33] is used. In addition, the user can emit commands to the system. This is implemented by a php-script accessed from the web interface. The php-script then triggers start or stop of a JavaScript in *dimctrl*. Form elements defined in the structure-files allow to customize the executed action by the user sending additional data to *dimctrl*.

## 5.2.7 Automation/Scheduling

Using the JavaScript interface with data-base access, automatic operation based on a pre-defined scheduling is currently under development and being tested. In a first step, the nightly schedule will be retrieved from a database and operations will take place accordingly. To fill the database in advance, a graphical web-interface is available, which allow to easily adapt the schedule on a nightly bases and acts as an archive for past schedules. For each night, plots are available which simplify scheduling, such as the zenith angle of each source versus time. Sources and times can be entered manually or be changed by checkboxes on a list of visible sources and sliders displayed in the plots.

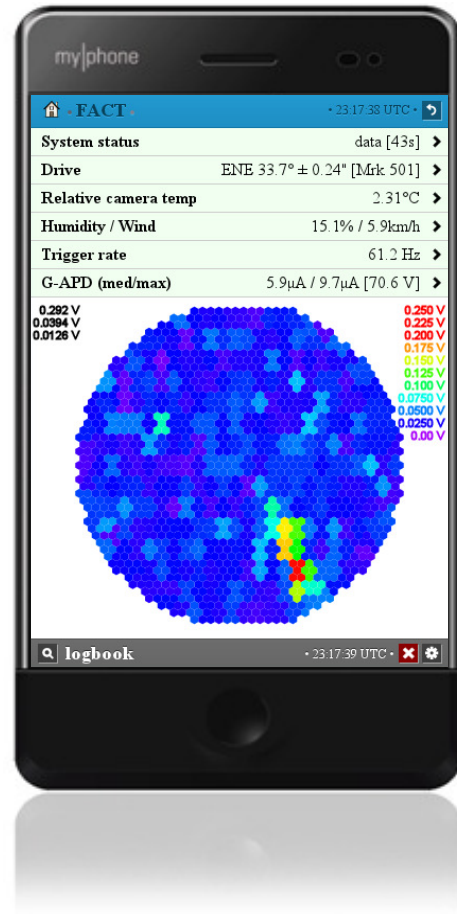


**Figure 18.** Screenshot of the Smartfact web-interface during data-taking. To maintain a low network traffic only an average value per bias-voltage channel is transmitted and displayed instead of one value per pixel.

### 5.2.8 Electronic Logbook

As a shift logbook the MyBB forum software [34] is installed. Each nightly shift is realized as a single thread. The advantage is that no special maintenance is necessary and standard software can be used. After or even during the shift other collaboration members can directly comment on logbook entries simplifying the later interpretation for the person in charge of data analysis. With some installed extensions, MyBB directly offers an overview calendar, easy editing (markdown language), a version for mobile devices, user authentication through the global LDAP password and marking entries as different priority. A possibility to add images or other documents and a search function is provided. Individual access rights can be customized to a large extend. The personal authentication system allows to keep easily track of the origin of each entry. Other forum categories offer the possibility to store related information within the same framework.

### 5.2.9 Individual Programs

Individual hardware components are controlled by eight programs. The 40 digitizer boards, the trigger master board and the slow-control board are controlled by *fadctrl*, *ftmctrl* and *fsctrl*, respectively, over custom Ethernet protocols. The bias voltage supply is controlled by the *biasctrl* over USB. Two Arduino-based boards controlling the power switches and the lids are operated via a simple built-in web-server from *pwrctrl* and *lidctrl*. The received HTML is parsed using Qt 4's HTML parser. To be able to re-use the MAGIC control software for the drive system, the *drivectrl* mimics the MAGIC slow control communication. The temperature dependence of the G-APD response is compensated by the *feedback*, using as input the readings from 31 temperature sensors in the sensor compartment. These values are distributed by the *fsctrl*. Taking the current readings for all 320 bias voltage channels, it also corrects the applied voltage for the corresponding voltage drop in the system. At the beginning of the data-taking the internal resistance of each channel of the bias power supply is calibrated. A *ratecontrol* adapts the over-all trigger threshold at the beginning of each run to the current light conditions. During the run, outliers induced by, e.g., reflections of bright stars are treated individually to keep the data rate reasonably low. The Master Control Program (*mcp*) coordinates all actions necessary to configure and start runs of different run-types. Ratescans measuring the dependence of the camera trigger rate from the trigger threshold are controlled by a *ratescan* program.

Additional auxiliary information is received from the weather station of the TNG telescope and the weather station of the MAGIC telescope by accessing their web-pages with *tngweather* and *magicweather*, respectively. The TNG web-page features XML data which is parsed using the Soprano library [35].

A special server is the *skypeclient* which communicates over Skype's DBus interface [36] with an open skype client. This allows the control of a skype session remotely and allows sending of alarm SMS in case of important alerts. Even ringing a phone is possible.

### 5.2.10 Feedback

Several ohmic resistors in series (shunt, output protection, cable, filter and bias resistors) introduce a voltage drop between the bias voltage supplies and the G-APDs depending on the current flow. The drawn current varies with the level of the diffuse night-sky background light in all channels,

and due to bright stars in individual channels. Since most G-APD properties depend on the applied voltage, a voltage correction is necessary. The feedback resistor of the HV operational amplifier of each bias voltage channel is calibrated by measuring the current for a set-point 3 V below the G-APDs breakdown voltage, thus no more operating the diode in Geiger-mode. Correcting the measured currents for the current loss at the parallel resistance, the voltage drop at each G-APD is calculated. The feedback program increases the applied voltage accordingly until the voltage calculated at the G-APD reaches the desired set-point. Included in this procedure is a linear correction of the gain changes induced by the temperature dependence of the G-APD. As reference, the average measured temperature in the sensor compartment is used.

### **5.2.11 Ratecontrol**

The trigger system measures the trigger rate of each of the 160 comparator outputs (patch rates) and the trigger rates at the output of the 40 N-out-of-4 logic (board rates). Since the N-out-of-4 circuit is also sensitive to the width of the input signal, electronic-noise induced triggers are filtered out and therefore patch and board rates are not exactly correlated.

At the beginning of each run, the median trigger rate of all board rates is regulated such that the accidental trigger rate induced by NSB is well below the trigger rate induced by charged particles. This step intentionally ignores single patches with higher rates as an effect of bright stars. The resulting threshold is kept constant throughout one run (usually 5 min) to ensure a stable energy threshold during each run. During the run, individual boards with exceptionally high trigger rates are identified and the threshold is increased for the patch with the highest trigger rate within that board. For every patch with an increased threshold and a trigger rate well below the limit for regulation, the threshold is decreased.

## **5.3 Data Acquisition**

As described in section 4.3, the camera contains 40 digitizer boards distributed over four crates. Each board reads out 36 pixels and is equipped with a commercial 100 MBit Ethernet interface delivering a maximum sustained throughput of 7 MB/s. Inside the camera there are two commercial low-power smart Ethernet switches (D-Link DGS 1224T), both having two 1000 Mbit fiber and 22 100/1000 Mbit copper connections. The switches are configured such that each crate has a dedicated fiber assigned. This ensures that the maximum sustained data rate deliverable by all boards does not overload the bandwidth of one fiber. The two other boards with an Ethernet interface, namely the trigger master and slow control board, are connected to the remaining copper connectors. For all Ethernet connections between the boards and the switches, slim cables of type Wirewin Cat.6 UTP are used. The data transmission from these switches to the backplane of the camera, and from there to the counting house, is done using optical fibers (Huber + Suhner, Masterline). In the counting house the fibers are connected to two more Ethernet switches of the same type having all computers needed to communicate with the camera connected to them. Even in case one of the two fiber pairs coming from the camera would fail, the system could be operated (at reduced performance). In figure 19 an overview of the architecture is shown. In addition, all computers in the counting room are connected to an internal network for data exchange.

The Data Acquisition (DAQ) computer (and its spare equivalent) has four dedicated 1000 Mbit Ethernet ports to communicate with the camera. All switches, as well as the ports of the computer,

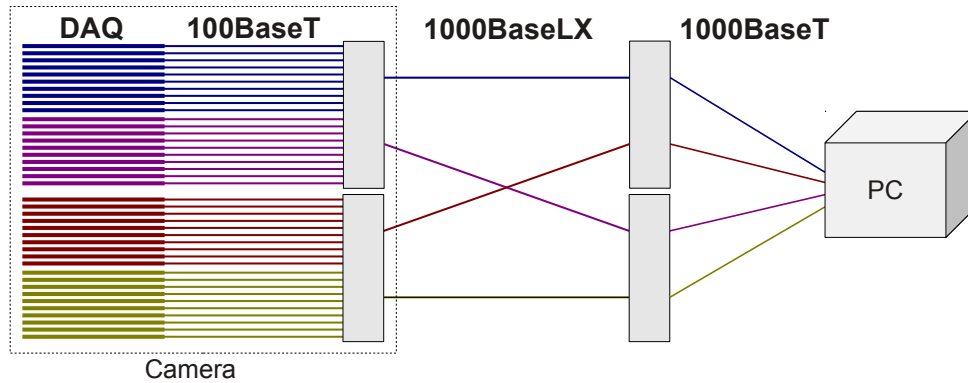


**Figure 19.** Overview of the FACT data acquisition system. From left to right four crates (10 boards each), the switches inside the camera, the switches in the counting house and the data acquisition computer are indicated. On the top, the Ethernet connection standard is given.

are configured to provide a bandwidth of 1000 Mbit between the computer and the camera, individually for all four crates. This allows to reach the maximum transfer rate of 7 MB/s to each of the 40 digitizer boards. Tests have shown that a sustained bandwidth between the camera and the computer exceeding 250 MB/s can indeed be maintained for extended time periods. When all 1024 samples per channel are read out, this bandwidth allows a sustained data rate corresponding to an average trigger rate of 70 Hz. When only 300 samples are retrieved, a trigger rate of 230 Hz can be achieved. This is well above the expected physics trigger rate for a telescope with a 9.5 m<sup>2</sup> mirror area. Ethernet interfaces and components with a ten times higher performance could have been integrated, but they would have had a significantly higher power consumption and would not have been necessary. Therefore these ideas were discarded.

Each of the 40 digitizer boards sends its data asynchronously to the computer, adding a header with additional information as a continuous event number. Based on this header information, a multi-threaded event builder program collects the data for one event from the different boards and writes the complete events to disk. In order to reduce in the future the amount of data written to disk, the event builder has already been prepared to apply a software trigger. Studies on an optimal trigger algorithm are ongoing.

## 5.4 Data Taking Procedure

Data taking is currently automated using batch scripts of commands executed by *dimctrl*. In this way, data integrity and data consistency can be ensured. Recently, scripts written in JavaScript are being implemented which allow a more complete automation like automatic error handling and retrieval of the schedule from an external source.

After power-on of all components, several checks are performed ensuring that all components got properly initialized. In particular, this is necessary for all components equipped with the Wiznet Ethernet chip, for which, due to a bug in the chip, sometimes negotiating of the connection speed with the connecting switch fails. This would result in unstable network connections. Subsequent to a proper initialization, a first DRS calibration is performed. For this, runs are taken with pseudo-random triggers with the G-APD bias voltage switched off. They are used to calibrate offset and



gain of each capacitor as well as a special offset introduced during readout into each logical sample. A special run digitizing a square signal is used for calibrating the timing behavior of each sample. Data taking is then started with the pseudo-random trigger and bias voltage on, while keeping the lids closed. This way the G-APD properties can be cross-checked by extracting their single-pe spectrum [41].

Observation of sources is currently carried out in two repeated blocks, each consisting of four runs with a duration of five minutes. For each observation, a dedicated DRS calibration is taken to account for temperature changes during the night. Each block is preceded by a pseudo-randomly triggered pedestal run and a light-pulsar run to have a cross-check reference for baseline and gain calibration. Each run is interleaved with pedestal and light-pulsar events at a rate of 1 Hz. Currently, 150 ns sampled with 2 GHz are recorded in each event. During each night, at least one ratescan is recorded for a continuous monitoring of the atmospheric conditions as well as the performance of the system. Ratescans and other special technical measurements are also automated by batch scripts.

Offline tools to easily access the data in the FITS files from the console and display the raw data as well as summary data (e.g. maximum value in the pipeline) are available.

## **5.5 Data Center**

After being recorded, the raw data are compressed using `gzip` to save disk space. Afterwards, files are automatically copied to the data center at ISDC and backed up from there to the data center in Würzburg. Already on-site at La Palma, quality as well as consistency checks are carried out. Information on the data and their quality are extracted from both, the raw and auxiliary data, and inserted to a MySQL database, from where they can be queried via a web interface. The stored values are later on used in the data selection for the physics analysis. At ISDC, again data consistency checks are performed before the validated data files are inserted into an archive. From this archive all data can be downloaded in FITS format. Further automatic processing steps have already been implemented, like calibration, signal extraction, image cleaning and calculation of image parameters. Also the Monte Carlo production and processing is already automatized.

## 6. Conclusions

During the past years, the first Cherenkov telescope using solid-state photosensors, Geiger-mode Avalanche Photodiodes, has been designed, built and set up by the FACT collaboration (see also [37, 39, 38]). It is in operation since Oct. 2011, c.f. [40].

As telescope structure, the mount of the previous HEGRA array is in use. Its 32 old mirrors have been replaced by refurbished mirrors with an about 10% larger reflective surface, 9.51 m<sup>2</sup> in total. The mirrors were measured to have a peak reflectivity of about 90%. The drive system has been replaced with a state-of-the-art drive system as applied on both MAGIC telescopes. The focal distance is 4.9 m yielding  $F/D \approx 1.4$ .

All necessary electronics, except the power supplies, are integrated in the camera body resulting in a total camera weight of about 150 kg. A passive water-cooling is applied. The total power consumption of the camera electronics is less than 0.5 kW.

The camera has a total disc-like field-of-view of 4.5° composed of 1440 pixels á 0.11°. Each pixel is equipped with a G-APD and a solid light concentrator (cone), made of plexiglass by injection molding, and glued to a protective front window. The grid distance of the hexagonal pixels is 9.5 mm. While the sensitive area of each G-APD is a square of 9 mm<sup>2</sup>, the cone exit area is 7.8 mm<sup>2</sup>. The cones were measured to have a peak transmission of 98% and the G-APDs have a peak photon detection efficiency (PDE) of ~33%.

The signal of nine pixels is summed to form a single trigger patch. Patches are arranged on an ideal hexagonal grid (see [20]). Before discrimination, clipping (shortening of the signal in time) is applied. As a noise filter, an additional N-out-of-4 logic is applied on the sum of four of the sum-signals. The trigger signal is distributed to the readout electronics, which are based on the DRS 4 ring-sampling chip allowing a time jitter between different channels as low as about 300 ps (depending on the sampling frequency). Each trigger patch is sub-divided into a compact four-pixel and five-pixel group. The G-APDs in one of the sub-groups share the same bias voltage, so in total 320 bias voltage channels are used.

### 6.1 Problems during Construction, Final Tests, and Operation

The industrial production of the light concentrators turned out to be more challenging than anticipated. Together with the producer the quality had to be improved gradually, and several selection measurements were necessary. Also the glueing of the concentrators to the G-APDs required some test runs and manual work. However, it should be noted that the primary goal was not to study or develop automated mass production techniques, but to equip the 1440 pixels of the FACT camera with light concentrators in a reasonable time.

After assembly of the camera, three pixels have been found dead thus delivering no signal at all. Since access to the sensor compartment is very difficult due to limited space, it was decided that the corresponding 2‰ loss is acceptable. Another three pixels were identified to have a too high bias-voltage, most probably due to a wrong serial resistor. They are switched off for the trigger during normal operation. Like for the dead pixels, it was decided that repair works would take too long and compromise the project start before winter. Furthermore, three patches with one signal short-cut between two neighboring pixels were identified. Since these twin-pixels deliver an

average signal, no influence on the trigger could be found. For data-analysis they act like a locally slightly larger pixel. Due to the high granularity of the image, no strong influence could be found.

During 1.5 years of operations, five hardware problems happened. Once, the firmware of the bias power supply got lost and had to be reprogrammed. A reason could not be identified. In summer 2012, the fuse of a DC-DC converter board in the camera blew. Since no obvious reason could be found, the origin might have been the fuse itself. This was fixed a few days later by an access to the camera. In winter 2012/2013, one bias voltage channel broke. Replacing the board in the power supply fixed the problem. Furthermore, a few times the clock conditioner on the trigger master board did not lock correctly after the startup of the camera electronics. To avoid lengthy multiple reboots, it was decided to keep the camera electronics powered all the time (in standby). The fifth problem was a bad cable connection inside the cabinet of the drive system (in the counting room). It should be emphasized that all of the above-mentioned problems are not related to the G-APDs.

## 6.2 Achievements

For the first time, an IACT not using classical PMTs, but G-APDs, for photon detection has been constructed and put into operation. The applied photo sensors were ordered off the shelf and have proven to be all within their specifications. The precision of each device and the measurement of the breakdown-voltage provided by the manufacturer was good enough that they could easily be sorted and a single voltage can be applied to several sensors at once. Keeping the overvoltage constant and homogenous throughout the camera during data taking could be achieved by a simple voltage adjustment, based on the consumed current and the ambient temperature. Details are discussed in a dedicated performance paper [41].

The readout system has single-p.e. resolution. More details on that can be found in [41]. A timing resolution of about 600 ps has been achieved for signals in the order of 5 p.e., including contributions from the whole signal chain (e.g. from the mirrors and the DRS chips). The precision of the trigger chain is comparable to the single-p.e. resolution of the readout chain, visible when measuring the trigger rate of a single pixel (all pixels except one switched off in a trigger patch) versus the comparator threshold, as shown in figure 20 (left).

Measurements of the total trigger rate versus comparator threshold, taken during dark nights (see figure 20, right) as well as moonlit nights, show the expected behavior and prove that the trigger works well. For a reasonable threshold, a rate in the order of 50 Hz–60 Hz is achieved during data taking. Some example events are shown in figure 21. In order to adapt the trigger thresholds to different light conditions, a rate-control has been implemented keeping the camera response homogeneous and stable through single data-taking runs.

Keeping the sensor and trigger response stable and homogeneous, first physics results have been obtained and published in [42]. Except for the above-mentioned minor problems, the operation of the telescope is stable since the moment it was put into operation. First air shower events were recorded immediately after the installation of the camera [40].

The consistent concept of the slow-control software features a robust and stable operation software-wise. A powerful local graphical interface is available for telescope and camera monitoring and control. A web-based interface with low bandwidth requirements has been implemented

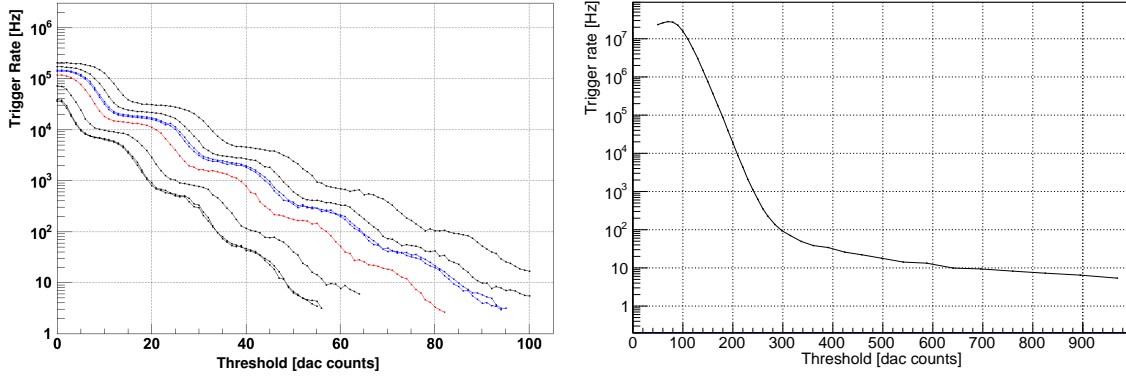


**Figure 20.** Left: Trigger rate in Hz versus comparator threshold in dac-counts with shutter closed. For this measurement, all pixels except one have been switched off in the trigger branch. Different curves were taken with different bias voltages applied. In all cases, the single-p.e. response is visible. Right: Overall camera trigger rate in Hz versus comparator threshold in dac-counts taken during dark night and good weather conditions. The trigger rates below a threshold of about one hundred dac-counts are influenced by saturation effects. Up to about 250 dac-counts, triggers of coincident photons from the diffuse night-sky background dominate. Above a threshold of about 300 dac-counts, triggers from hadron-induced air-showers dominate. The slope of the hadron branch exhibits a good correlation with the slope expected from the proton spectrum.

for remote operation. Telescope control is available through a JavaScript interpreter and fully automatic operation is already in the test-phase. A first automatic data-analysis running on site is available and can soon be used to deliver triggers for target-of-opportunity observations to other observatories. Data is written in a self-explanatory format (FITS), with the goal to make it publicly available.

### 6.3 Possible Future Improvements and Outlook

Although the telescope is working very reliably, still some improvements can be implemented. On the hardware side, this is mainly an alignment system for the mirrors, which is currently in the design phase. On the software side, this is the implementation of a software trigger to suppress background events triggered from night-sky background. Another possibility is to upgrade the system such that the voltage applied to the G-APDs is adjusted without involving a computer in the control loop. However, since this equires not only a new firmware for the controller in the supply crate, but also a re-design of the hardware, it will probably not happen in the near future.

A nearly complete remote operation of the telescope has already been achieved. Currently under development is the automated operation. First tests of the system have already been performed and automatic operation will start within the coming months. Of course, robotic, i.e. self-sustained, operations are limited by a hardware not primarily build for this purpose, so that the need for a remote shifter during night is still expected.

Geiger-mode avalanche photodiodes (G-APD) have turned into a great option for Cherenkov telescopes, in particular also for the CTA project [43]. They have kept their promise to be easy to handle and to allow for a very stable operation also during moontime conditions. Even though production of solid light concentrators, and their glueing process, needs further investigation to be considered for mass production, the FACT concept has turned out to be a benchmark for future

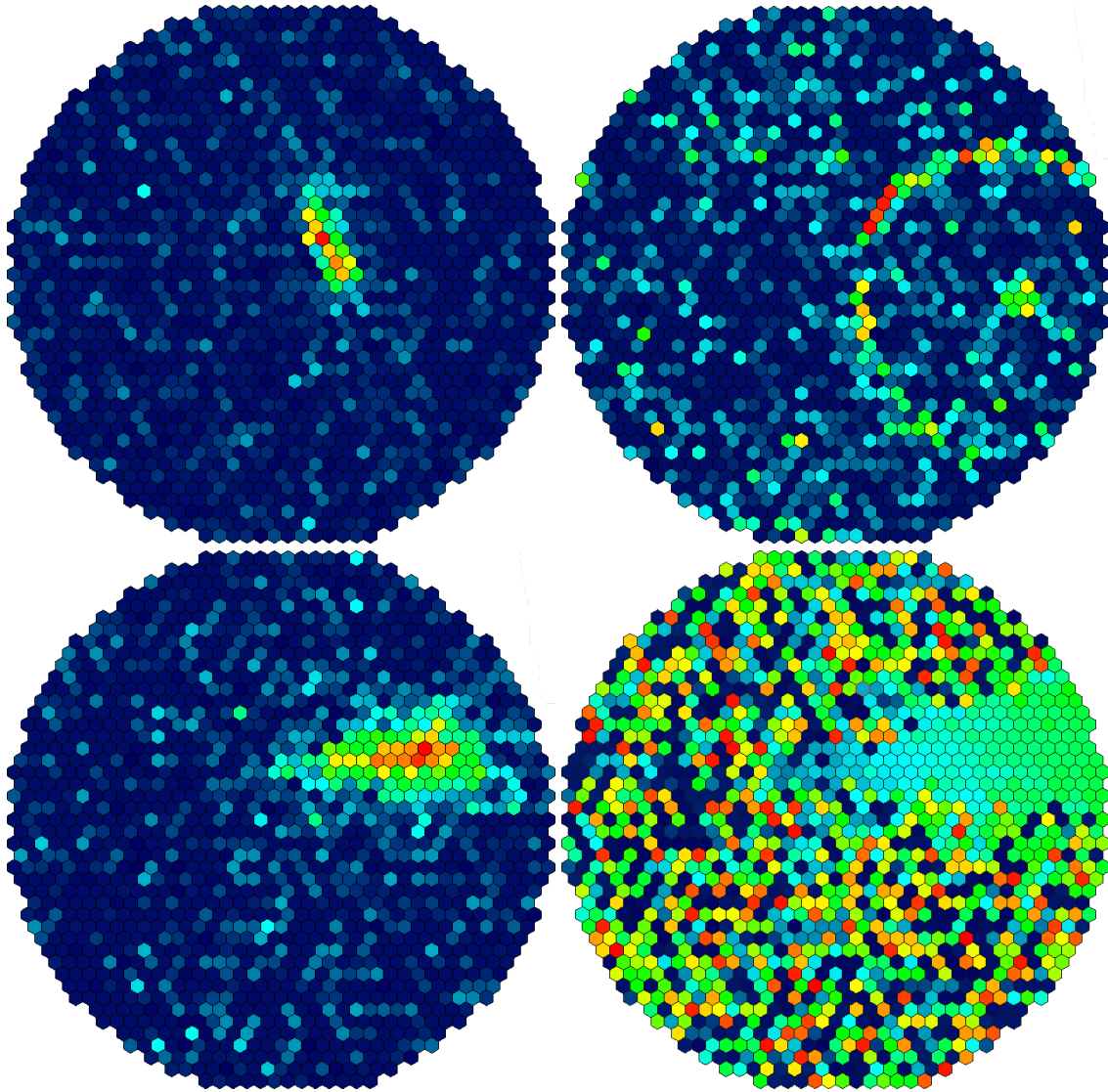


**Figure 21.** Examples of air shower images recorded by FACT. The two images at the top correspond to a gamma candidate and a muon event, with the color code representing the pixel amplitude. At the bottom a proton shower is shown, both in amplitude (left) and signal time (right).

Cherenkov telescopes. Considering the fast drop in price for solid state devices (today's price for G-APDs is already about a factor of ten lower than when the devices for FACT were bought), the construction of the FACT camera has proven that monitoring of the brightest sources with single Cherenkov telescopes becomes affordable and that 24/7 monitoring on long-terms is possible.

Source monitoring with FACT has already been on-going since the installation of the camera, thus during the commissioning of the instrument. In the future the priority will be the stable and uninterrupted operation of the system to ensure continuous long-term monitoring of the brightest known blazars [2] and to act as a flare-trigger for other telescopes.

## Acknowledgments

The important contributions from ETH Zurich grants ETH-10.08-2 and ETH-27.12-1 as well as the funding by the German BMBF (Verbundforschung Astro- und Astroteilchenphysik) are gratefully acknowledged. We thank the Instituto de Astrofísica de Canarias allowing us to operate the telescope at the Observatorio Roque de los Muchachos in La Palma, and the Max-Planck-Institut für Physik for providing us with the mount of the former HEGRA CT 3 telescope. We also thank the group of Marinella Tose from the College of Engineering and Technology at Western Mindanao State University, Philippines, for providing us with the scheduling web-interface.

## References

- [1] E. Lorenz and R. Wagner, *Very-high energy gamma-ray astronomy: A 23-year success story in high-energy astroparticle physics*, *Eur. Phys. J. H* **37(3)** (2012) 459 [astro-ph/1207.6003].
- [2] T. Bretz et al., *Long-term monitoring of bright blazars with a dedicated Cherenkov telescope*, *AIP Conf. Proc.* **1085** (2008) 850.
- [3] T. C. Weekes et al., *Observation of TeV gamma rays from the Crab Nebula using the atmospheric Cherenkov imaging technique*, *Astrophys. J.* **342** (1989) 379.
- [4] A. M. Hillas, *Cerenkov light images of EAS produced by primary gamma rays and by nuclei*, *Proc. of the 19th Internat. Cosmic Ray Conf.* **3** (1985) 445.
- [5] R. Mirzoyan and E. Lorenz, *Measurement of the night sky light background at La Palma*, *Report MPI-PhE* **94-35** (1994), Max Planck Institute for Physics, Munich.
- [6] D. L. King, *Atmospheric extinction at the Roque de los Muchachos Observatory*, *La Palma technical note* **31** (1985).
- [7] D. Renker and E. Lorenz, *Advances in solid state photon detectors*, 2009 *JINST* **4** P04004.
- [8] H. Anderhub et al., *A novel camera type for very high energy gamma-ray astronomy based on Geiger-mode avalanche photodiodes*, 2009 *JINST* **4** P10010.
- [9] The MAGIC telescopes, <http://magic.mppmu.mpg.de>.
- [10] A. Daum et al., *First results on the performance of the HEGRA IACT array*, *Astropart. Phys.* **8** (1997) 1.
- [11] A. Konopelko et al., *Performance of the stereoscopic system of the HEGRA imaging air Cherenkov telescopes*, *Astropart. Phys.* **10** (1999) 275 [astro-ph/9901199].
- [12] T. Bretz, D. Dorner, R. M. Wagner and P. Sawallisch, *The drive system of the major atmospheric gamma-ray imaging Cherenkov telescope*, *Astropart. Phys.* **31** (2009) 92 [astro-ph/0810.4593].
- [13] J. M. Davies and E. S. Cotton, *Design of the Quartermaster Solar Furnace*, *J. Solar Energy, Sci. Eng.* **1** (1957) 16.
- [14] Refractive Index Database, <http://refractiveindex.info>.
- [15] Hamamatsu Photonics K. K., <http://www.hamamatsu.com>, *MPPC data sheet* (2008).
- [16] A. N. Otte, *On the efficiency of photon emission during electrical breakdown in silicon*, *NIM A* **610(1)** (2009) 105.



- [17] I. Braun et al., *Solid light concentrators for Cherenkov astronomy*, *Proc. of the 31st Internat. Cosmic Ray Conf.* (2009); new publication in preparation.
- [18] T. Kraehenbuehl et al., *Geiger-mode avalanche photodiodes as photodetectors in Cherenkov astronomy*, *Proc. Sci.* **PD09** (2009) 024.
- [19] B. Huber et al., *Proc. of the 32nd Internat. Cosmic Ray Conf.* (2011).
- [20] H. Anderhub et al., *Electronics for the camera of the First G-APD Cherenkov Telescope (FACT) for ground based gamma-ray astronomy*, 2012 *JINST* **7** C01073.
- [21] S. Ritt, R. Dinapoli and U. Hartmann, *Application of the DRS chip for fast waveform digitizing*, *NIM A* **623(1)** (2010) 486.
- [22] Boost C++ libraries, <http://www.boost.org>.
- [23] Munin network and system monitoring, <http://munin-monitoring.org>.
- [24] Distributed Information Management (DIM) system, <http://dim.web.cern.ch>.
- [25] W. D. Pence et al., *Definition of the Flexible Image Transport System (FITS), version 3.0*, *Astron. Astrophys.* **524** (2010) 42.
- [26] NASA's HEASARC software, CCfits, <http://heasarc.gsfc.nasa.gov/fitsio/CCfits>.
- [27] Zlib compression library, <http://www.zlib.net>.
- [28] R. A. Shaw, H. E. Payne and J. J. E. Hayes, *Astronomical Data Analysis Software and Systems IV*, *ASP Conf. Ser.* **77** (1995).
- [29] V8 JavaScript engine, <http://code.google.com/p/v8>.
- [30] Qt application and development framework, <http://qt.digia.com>.
- [31] CERN's ROOT library, <http://root.cern.ch>.
- [32] OpenGL for high performance graphics, <http://www.opengl.org>.
- [33] Nova environment for astronomers, <http://nova.sourceforge.net>.
- [34] MyBB forum software, <http://www.mybb.com>.
- [35] Soprano software for RDF data, <http://soprano.sourceforge.net>.
- [36] Skype API reference manual, <http://developer.skype.com/desktop-api-reference>.
- [37] H. Anderhub et al., *Results of the prototype camera for FACT*, *NIM A* **639** (2011) 58.
- [38] Q. Weitzel et al., *FACT: A Novel Camera for Cherenkov Telescopes for Ground-Based Gamma-Ray Astronomy*, *Conf. Rec. IEEE Nucl. Sci. Symp.* (2011) 1857.
- [39] T. Bretz et al., *A status report: FACT – a fact!*, *Proc. of the 13th ICATPP Conf., World Sci.* **7** (2012) 29.
- [40] Cern Courier **10** (2011) 6, <http://cerncourier.com/cws/article/cern/47816>.
- [41] H. Anderhub et al., *Stability of G-APD properties in the FACT camera*, in preparation.
- [42] T. Bretz, D. Dorner et al., *FACT – The first G-APD Cherenkov telescope (first results)*, *AIP Conf. Proc.* **1505** (2012) 773.
- [43] The Cherenkov Telescope Array (CTA), <http://www.cta-observatory.org>.